Nuclear and molecular imaging modalities for predicting calcific aortic valve disease progression in animal models

Gedaliah Farber

Thesis submitted to the University of Ottawa
in partial Fulfillment of the requirements for the
MSc in Biochemistry

Department of Biochemistry
Faculty of Medicine
University of Ottawa

Abstract

Introduction and Objectives Calcific aortic valve disease (CAVD) is the most common valvular disease, accounting for 50% of all valve disorders and is the third most common cardiovascular disease following coronary disease and hypertension.[1,2] Currently, there is no pharmacological agent capable of reversing or slowing down the progression of CAVD and treatment of severe cases consists of surgical repair or valve replacement[2]. Hence, there is a crucial need for earlier detection using predictive biomarkers that will allow for preventative intervention as opposed to post-symptomatic disease treatment or management.

Namely, one target of particular interest is the expression of matrix metalloproteinases (MMPs) (specifically MMP-1, -2, and -9) which are upregulated in CAVD prior to calcification events and have been previously shown to serve as an attractive molecular imaging target.[1–3]

The primary objective of this study is to assess the feasibility of detecting biomarkers of CAVD by various *in vivo* imaging modalities, such as PET and echocardiography. In addition, this study assesses disease progression in various mouse strains to qualify an appropriate CAVD animal model.

Methods In vivo and ex vivo imaging of C57Bl/6 and ApoE$^{-/-}$ (n = 8 per strain cohort) mouse models are used to link unique features of matrix remodelling with CAVD progression. At baseline and longitudinal follow-up (4, 8, and 12 months), in vivo hemodynamic impairment is assessed through echocardiography, and calcification and MMP activity are measured using PET with a series of radiotracers: [^{18}F]NaF for calcification, [^{18}F]BR351 for the molecular targets of MMP-2 and -9, and [^{18}F]FMBP with molecular target specificity for MMP-13. Following imaging, aortic valve (AV) tissue is harvested, sectioned, and analyzed for calcification, inflammatory markers, collagen types, and MMP activity in AV leaflets. Tracer autoradiography, immunofluorescence, and *in situ* zymography are used to confirm in vivo imaging results with improved resolution and quantification in valves. Histological sample preparation, experimentation, and analyses are then repeated in human AV tissue samples for relative comparison of biomarker expression in animal models.

Results Echocardiography suggests positive signs of disease progression in experimental animal models. In comparison to WT, ApoE$^{-/-}$ mice show: increased peak velocity ($p<0.0001$), decreased aortic valve area ($p<0.001$), and irregular valve dynamics. [^{18}F]NaF PET imaging shows expected bone uptake and low calcium-burden in young and WT animals. [^{18}F]FMBP shows increased uptake in the valve area of diseased models at later timepoints, 1.530 compared to <0.001 %ID/g ($p<0.005$), in disease vs control animals respectively. Furthermore, confirmation of sought-after biomarkers has also been assessed by analysis of various histological sample preparations including the presence of leaflet calcification, upregulation of MMP-2, -9, and -13, matrix remodelling, lipids, inflammatory markers, and activated MMP expression.

Conclusion Findings from this study suggest that molecular imaging techniques using target-specific radiotracers, as well as echocardiography for assessment of hemodynamic impairment, are feasible solutions in predicting disease onset in CAVD specific animal models.

Acknowledgements

I would like to thank my phenomenal supervisor Dr. Benjamin Rotstein for affording me this opportunity as well as for his tutelage, guidance, and continued support throughout my studies in his lab. Dr. Rotstein's lab is always a positive and welcoming environment to work in. It has been truly an incredible experience to have such an impactful mentor play a critical role in furthering not only my abilities as a researcher but for also helping me work towards achieving my academic and professional goals. Thank you for always believing in me, seeing my potential, and always encouraging me to pursue my passions. I could not have asked for a better supervisor and friend.

I would also like to thank Xiaoling Zhao and Richard Seymour who helped me establish many of the sample preparations, histological methods, and echocardiography techniques that were integral to the success of this project.

Thank you as well to my thesis advisory committee Dr. Mireille Ouimet and Dr. David Messika-Zeitoun for their valuable input and guidance throughout my studies. Their combined expertise and unique perspectives has added immense value to not only my project but also my field as a whole.

Lastly, I would like to thank the rest of the members of the Rotstein lab, Animal Care and Veterinary Staff, and University of Ottawa Heart Institute team members for always being available as a resource and for assisting me in a lot of the work that goes on behind the scenes to make this project feasible. Everyone has been extremely supportive and I will always cherish the connections I have made as their colleague and peer.

COVID-19 Disclaimer

It is important to note that this research project was conducted over a two-year period (2018-2020) which, unfortunately, was interrupted in the latter half due to the COVID-19 pandemic. As a result, all ongoing studies had to be put on pause as facilities not directly working on pandemic-related research were deemed to be non-essential. The closure of the lab thereby impeded the completion of some of the studies and analysis necessary for completion of this project and have therefore been adapted or omitted from this thesis. These studies will be completed upon return to lab practice with appropriate COVID-19 physical distancing measures considered.

Thank you for your understanding during these uncertain and difficult times,

Gedaliah Farber

Table of Contents

List of Abbreviated Terms

ALP – Alkaline phosphatase

ApoE – Apolipoprotein E

AR – Aortic regurgitation

AS – Aortic stenosis

AV – Aortic valve

AVA – Aortic valve area

BAV – Bicuspid aortic valve

BMP – Bone morphogenetic protein

CAVD – Calcific aortic valve disease

ECM – Extracellular matrix

IAW – Inveon acquisition workplace

IHC – Immunohistochemistry

[^{18}F]NaF – Sodium [^{18}F]fluoride

[^{18}F]FDG – [^{18}F]2-fluoro-2-deoxyglucose

LDL – Low density lipoprotein

LN – Left-non-coronary

LRP5 – Low-density lipoprotein receptor-related protein 5

LVOT – Left ventricular outflow tract

MMP – Matrix metalloproteinases

OCT – Optimal cutting temperature

ORO – Oil Red-O

Ox-LDL – Oxidized low density lipoprotein

PBS – Phosphate buffered saline

PET – Positron Emission Tomography

PLAX – Parasternal long axis

PSAX – Parasternal short axis

PSR – Picrosirius red

RANKL – Receptor activator of nuclear factor kappa-B ligand

RL – Right-left

RLU – Relative light units

RN – Right-non-coronary

ROI – Region of interest

SPECT – Single photon emission computed tomography

TAC – Time activity curve

TAV – Tricuspid aortic valve

TBR – Tissue to background ratio

TGF-β – Tissue growth factor-beta

TEE – Transesophageal echocardiogram

TIMPs – Tissue inhibitors of MMPs

VEC – Valvular endothelial cells

VIC – Valvular interstitial cells

VTI – Velocity time integral

List of Figures

1.0 Introduction

1.1 Background

Calcific aortic valve disease (CAVD) is considered the most common valvular disease, accounting for 50% of all valve disorders and is the third most common cardiovascular disease following coronary disease and hypertension.[1] It is characterized by accumulation of calcium-phosphate deposits within the fibrous matrix of the aortic valve (AV) leaflets resulting in aortic stenosis (AS) and narrowing of the AV opening. As such, CAVD is considered a major public health concern with incidences expected to reach epidemic proportions as the aging population and life expectancy continue to increase.[1,4] Approximately 3% of people aged 65 and over will develop some degree of calcific AS, with half having an increased risk of adverse cardiovascular health outcomes.[5] Previously, CAVD had been thought of as a degenerative disease but, recently, the general accepted viewpoint is that the disease is of a progressive nature and shares many characteristics typical of skeletal bone formation.[6] This includes matrix remodelling which makes use of fibroblast-like, valvular interstitial cells (VICs) which are differentiated into osteoblastic and osteoclastic-like cells, expressing many of the same cellular markers (Appendix A – Figure 14).[5]

Currently there is no pharmacological agent capable of reversing or slowing down the progression of CAVD and treatment of severe cases consists of surgical repair or replacement valve therapies.[7] Hence the need for earlier detection through predictive biomarkers which will allow for preventative interventions as opposed to disease treatment or management which may be associated with greater risk factors, poorer prognoses, and elevated healthcare costs.

1.2 Risk Factors

In referencing the literature various predisposing risk factors which may make one more susceptible to developing CAVD become apparent. This includes general factors such as genetics, environment, age, male sex, as well as lifestyle and other pathologies such as atherosclerosis, presence of oxidised low density lipoproteins (ox-LDLs), diabetes mellitus, hypercholesterolemia, and hypertension.[2,5,8] One of the greatest risk factors involved in the development of CAVD however, is the presence of a bicuspid aortic valve (BAV).[9,10] Of the environmental factors, there is a high degree of overlap with other vascular diseases such as atherosclerosis.[11] Hence the need to focus on more genetic and hemodynamically significant contributions to disease etiology as they may serve as better predictors for disease specific progression.

1.3 Valvular Interstitial Cells

The main cell types of the AV, and which are the most likely to be implemented in the pathogenesis of CAVD, are the VICs. These cells are thought to be involved in the fundamental process of extracellular matrix (ECM) remodelling and mineralization seen in CAVD. Although these cells have been studied for many years, there still remains several uncertainties in the exact mechanism involved by which they progress toward a state of calcification. First what should be highlighted is the progression of these resident cells and how they differentiate into osteoblast-like cells. Their unique function and characteristics can take multiple different forms depending on what phenotype they express and what degree of differentiation (forward or backwards) they have undergone while all existing in

the same space simultaneously.[12] For that reason, they have been categorized as either: embryonic progenitor endothelial/mesenchymal cells, quiescent VICs, activated VICs, progenitor VICs, or osteoblastic VICs.[12,13]

The first class of VICs, the embryonic progenitor endothelial/mesenchymal cells, are the least important in regard to CAVD progression as their role is fairly limited to the formative period of the AV in embryogenesis.[12,14] Their main function is to facilitate the translation of endothelial cells of the endocardial cushion to mesenchymal cells and are heavily influenced by a myriad of developmental genes and regulatory pathways working in unison (see section 1.4).[13]

In the adult population, however, the predominant cell type are the quiescent VICs which are responsible for valve function by constantly supplying the necessary components integral to maintaining regular AV function and structural integrity.[13] When these cells are exposed to stressors their role shifts and there is an increased function in tissue repair, thereby classifying them as activated VICs.[13,14] Previously, it was believed that in the response to injury, there was a marked increase in the number of VICs proliferating or that there is a regulatory mechanism in place to decrease the degree of apoptosis during valvular remodelling.[13] The now more widely accepted rationale is that there is a secondary method by which activated VICs are recruited. This being by the presence of progenitor VICs, a type of valvular stem cell, which aids in the process of repair by converting to the activated VIC form or by initiating a paracrine signalling cascade to recruit other progenitor cells.[13,15] These can take the form of either endothelial progenitor cells or dendritic cells and while this mechanism is still not well understood, it is thought that they both originate from a common circulating hematopoietic stem cell.[13,16–18]

Under physiological conditions, the valve is suited to cope with the normal mechanical forces it is exposed to on a continuous basis. When these forces become persistent or are exacerbated, the typically neutral state quiescent VICs shift to their activated form. The role of these activated VICs typically resembles myofibroblasts in how they function.[12,14,15] As previously mentioned, they arise predominantly from quiescent VICs exposed to stressors such as abnormal hemodynamics and mechanical stress or pathological injury.[13] This process involves the recruitment of valvular endothelial cells (VECs) and foam cells which ultimately results in increased ECM remodelling by coordination of matrix metalloproteinases (MMPs) and tissue inhibitors of MMPs (TIMPs).[19] This is a normal response to wound healing and after the VECs have served their function they are removed by apoptosis.[20] The maladaptive response arises when coordination of this process is lost and the AV experiences irregular ECM remodelling as a result of continuously activated VICs. This process ultimately leads to calcification.[12,20,21]

The last cell type to be discussed is the osteoblastic VICs. It should be noted however, that VICs can be induced to display not only osteogenic properties but also adipogenic, chondrogenic, and myofibrogenic lineages and that osteogenic properties are just one potential differentiation pattern for this cell type.[22] The osteoblastic VICs arise directly from quiescent VICs and these cells represent the end stage of disease progression and function in the promotion of calcium nodules.[13,22] It is important to highlight as well that there are certain characteristics as well which introduce variance in the observed degree of calcification between individuals within a population. For instance, it has recently been reported that male VICs are more susceptible to osteogenic-like patterns of behaviour.[23] In a 2017 study by Masjedi and colleagues, they showed that in rat and

porcine aortas cultured *in vitro*, while there was significantly increased proliferation of VICs in females over males, the male VICs showed significantly elevated biomarkers of interest (such as MMP-2 expression) and were more likely to form larger calcific nodules.[23] Considering osteoblastic VICs tendency to have a higher expression of proteins affiliated with osteogenesis and chondrogenesis, this provides invaluable insight to the various underpinning genetic and post-translational modifications and signalling cascades involved in the molecular mechanism of CAVD.

1.4 Molecular Mechanisms of Disease

The mechanisms by which CAVD occurs is a complicated and poorly elucidated culmination of various gene expressions, signalling cascades, and differentiation. Similarly to atherosclerosis, CAVD is characterized by hyperplasia of the basement membrane, invasion of an inflammatory immune response, cell infiltration, lipid deposition, and calcification (Figure 1).[10,11,14,24] While these other aspects of disease pathophysiology are important, in the interest of maintaining focus, only the end stage mechanism of calcification will be covered. Although there appears to be several overlapping factors and processes between CAVD and atherosclerosis, there is still a need to uncover the specific mechanisms by which mineralization of the AV occurs.[14]

With regard to calcification, it is thought that the activation of pro-osteogenic signaling cascades functions as the central mechanism responsible for calcific AS.[15] Of the osteogenic signaling cascades, one which is of particular interest is the bone morphogenetic protein (BMP) signaling cascade typically upregulated in calcified AVs (Figure 1).[15,25]

While the exact mechanism by which BMPs are recruited is not well understood, there is evidence to suggest that non-laminar flow patterns (such as valvular regurgitation) on the endothelial side of the valve aids in the propagation of BMP2/4 secretion.[25–27] As is seen in hypercholesterolemic mice, however, phospho-smad1/5/8, a staple in BMP signalling and a key feature of stenotic valves, increases preceding valve orifice area decline and is further increased in proportion to valvular impairment and calcification.[27–29]

Furthermore, aside from BMPs, one of the key mechanisms garnering attention is the mechanism of tissue growth factor-beta (TGF-β) which is also believed to play a role in differentiating VICs to their osteoblastic subtype as they are secreted by active VICs (Figure 1).[30] What has been previously shown is that the calcification process is highly dependent on the increased expression of alkaline phosphatase (ALP) activity.[15,28,31] This is important as TGF-β is involved in the regulation and coordination of ALP and promotes the calcification of the ALP-rich nodules it forms within the valve.[21,32] In addition, these calcified nodules have shown to produce hydroxyapatite, an attractive small-biological molecule from a nuclear imaging standpoint and a substrate for calcification (see section 1.7).[13]

The next molecular mechanism to focus on is the Wnt/β-catenin and low-density lipoprotein receptor-related protein 5 (LRP5) signalling cascade working both individually and in unison. Previously, Wnt and LRP5 have been shown to be critical in the process of valve development and skeletal bone formation, respectively.[33–36] This mechanism is derived by how Wnt and activated β-catenin bind to LRP5 to initiate skeletal bone formation.[37] Furthermore, it has been long established that ox-LDL plays a key role in the pathogenesis of CAVD.[33] It is believed that the ox-LDL, which

directly promotes valvular calcification, functions by stimulating these pathways by up-regulating GSK-3β, β-catenin, LRP5, and converting VICs to osteoblast-like cells.[30,33,34]

Lastly, the role and mechanism by which MMPs are involved in the pathology of CAVD is important to mention as well as it aids in providing the rationale for their use as a nuclear imaging target. But first, it is important to identify what MMPs are and how they function. MMPs are a class of endogenous calcium-dependent zinc-containing endopeptidases.[38] In the ECM, the pro-domain (consisting of a cysteine motif which maintains the inactivity of the catalytic site) is cleaved and thereby converted to the active form, working by degrading and remodelling the surrounding ECM while being highly regulated by TIMPs.[38,39]

With regard to CAVD, of particular interest are gelatinases and collagenases which are upregulated in early stages of the disease.[3,39] In terms of specific gelatinases involved, it is believed that MMP-2 and -9 exhibit the greatest expression while for the collagenases, MMP-1 is the MMP isozyme of interest.[3,40,41] As MMP-1 is not naturally expressed in mice, MMP-13 is used as a proxy due to its similar role and expression pattern in the model used for this study.[42] While the exact mechanism by which these endogenous proteins are recruited in disease pathogenesis is not fully understood, it has been well established that their function in matrix remodelling serves to accommodate inflammatory and calcification processes.[39] Interestingly, new evidence suggests that for MMP-2 specifically, it is seen to be upregulated in aortic sclerosis preceding valvular stenosis in comparison to normal healthy human valve tissue samples.[40] These clinical findings are supported in the preliminary data presented herein (Section 3.2). In

this respect, it is believed that they play a protective role with adverse consequences arising when control over this mechanism is lost or unable to keep up with the rate and demand of remodelling.[13,39]

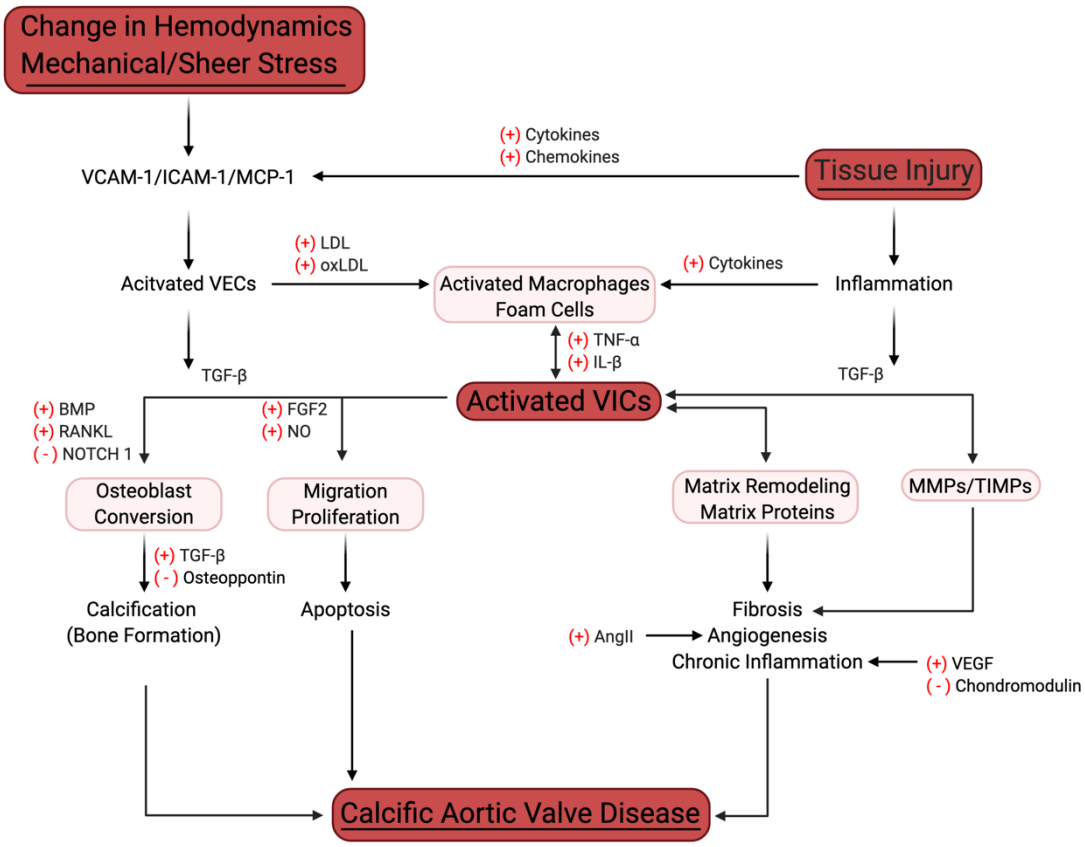

Figure 2: Molecular Mechanisms of CAVD
The proposed molecular mechanism of CAVD is a complicated and still poorly understood culmination of various molecular and genetic pathways working in unison. Starting with initiating stressor event in the valve such as disruption of normal hemodynamics and tissue injury, a cascade of proteins and inflammatory markers are released. These are free to interact with other cells present in the valvular space and ultimately lead to the sequestering of activated valvular interstitial cells (VICs). From here, other biomarkers such as bone morphogenic protein (BMP), and receptor activator of nuclear factor kappa-B ligand (RANKL) are upregulated while inhibition of others such as NOTCH 1 to convert activated VICs to osteoblastic VICs; ultimately leading to valvular calcification. (+) indicates upregulation, (-) indicates downregulation. Adapted from Liu, Joag, and Gotlieb.[13] Made with Biorender©.

1.5 CAVD Animal Models

Of the aforementioned predisposing risk factors, genetics is of particular interest as it presents the opportunity for a mutagenic animal model specific to CAVD. Previously, research groups have used apolipoprotein E knockout ($ApoE^{-/-}$) animals models on high-fat diets in CAVD experiments.[43] The benefit of knocking out this gene is that it impairs the normal metabolism of lipids and subsequent removal of cholesterol from the bloodstream.[44] This results in an accumulation of lipids contributing to fat build up and arterial scarring.[45] Considering the overlap in pathologies between the two diseases it is apparent why using animal models commonly used in atherosclerosis research may present as an attractive model for CAVD as there is evidence which suggests the expression of calcification in atherosclerotic vascular lesions and aortic valves of these animals.[5] While there are advantages to using these models, in reality, it overlooks the caveats that as it is not disease specific and findings are inconsistent, specifically those related to calcification.[43] That being said, although this a known limitation of the animal model, it is still amongst the most widely used for CAVD imaging research.[3] Although there are many models which serve as a proxy for modelling CAVD in a similar manner to what is observed in a clinical setting, there is an evident need for a more CAVD-specific animal model. Recently, efforts have been made to attempt a CAVD-specific animal model by breeding mice to express a BAV phenotype as opposed to the typical tricuspid aortic valve (TAV) morphology.[9,46] These models can involve the altered expression of various genes involved in the formation of the AV during embryogenesis but one model garnering recent attention is the role of Gata genes. As shown by the Nemer lab at the University of Ottawa, *Gata5*$^{-/-}$ and *Gata6*$^{+/-}$ mice yield different phenotypes (right-non-coronary (RN) and right-

left (RL) fusion, respectively) and mechanistic features of human BAV in approximately 50% and 30% male and female experimental populations, respectively.[9,46] This acts as a model of significance as BAV is the most common congenital heart defect affecting 1-2% of the population and accounts for approximately half of all severe CAVD cases referred for surgery.[6] Within the BAV model three distinct fused subtypes exist and are classified as RL, RN, and left-non-coronary (LN) with RL being the most prevalent in humans accounting for approximately 75% of cases.[47] In studies carried out by the Nemer lab, they showed that like humans, the heterozygous *Gata6* phenotype mostly expressed the RL, BAV phenotype.[9]

Moreover, in a recent publication by Scatena et al., they made use of a diabetogenic animal model ($LDLr^{-/-}ApoB^{100/100}$) put on a high-fat, procalcific diet to show how it results in an increased incidence of CAVD.[1] Making use of echocardiography and various histological methods, the research group was able to show progression of aortic stenosis in their animal model as a longitudinal study and deposition of calcium in valve leaflets, respectively.[1] The animals placed on the procalcific diet had just over 75% incidence of hemodynamically significant AS with thickened and calcified AV leaflets in comparison to those fed normal rodent chow.[1]

Lastly, in a review published in 2011 by Sider, Blaser & Simmons at the University of Toronto, they note several other CAVD animal models (both rodent and higher order species) as well as guidelines for different diets to highlight and help advance specific features of disease the different strains develop.[43] It important to note, however, that while their list is extensive and comprehensive, the feasibility of working with some of the

models listed presents with other challenges such as extensive timelines, cost, and limited evidence.[43]

1.6 Imaging Modalities

In terms of *in vivo* animal imaging, one of the more beneficial modalities comes in the form of nuclear imaging using positron emission tomography (PET) and single photon computed tomography (SPECT).[48] Both modalities rely on fairly similar principles in that they convert gamma photons from decaying isotopes into electrical signals which are then reconstructed through various algorithms to produce a 3D image.[48] The difference between the two is that PET scanners rely on two gamma photons produced in an annihilation event reaching opposing detectors simultaneously whereas SPECT radiotracers only emit a single gamma photon.[48] Furthermore, PET radiotracers tend to emit at higher energies, requiring modifications to be made in the surrounding absorptive materials.[48] One of the major benefits of these nuclear molecular imaging modalities is that they provide a complementary approach to studying *in vivo* molecular mechanisms with a high degree of accuracy and specificity.

Another live-imaging modality which is starting to be used more frequently as superior image resolutions become available for small animal imaging is echocardiography. Transesophageal echocardiography (TEE) is capable of quickly acquiring an exceptional amount of relevant CAVD data such as valve morphology, area, pressure gradient, and leaflet cusp separation, all of which cannot be assessed by other conventional live-animal imaging modalities[15]. By favouring the use of echocardiography for predicting CAVD progression, the amount of radiation exposure one would receive by

other methodologies is significantly decreased. This also falls in line with standards of diagnosing CAVD and AS in a clinical setting. Measurements such as peak velocity, mean gradient, and aortic valve area (AVA) are all quantitative measurements that can be used to assess disease severity[15]. In severe cases, leaflet calcification can be assessed using echocardiography in clinic due to the brightly reflected, bone-like signal picked up by the transducer.

1.7 Radiotracers

One of the biggest challenges facing this area of research are the limitations existing with small-animal imaging modalities. To enable nuclear imaging, researchers have mostly used readily available radiotracers in attempt to visualize various CAVD biomarkers. With regard to PET studies, some of the more popular targets are AV leaflet calcification and disease-affiliated inflammation.[49,50] While valuable, these tracers are not predictive of disease outcome and face a range of pitfalls. Two such PET radiotracers used frequently are [^{18}F]2-fluoro-2-deoxyglucose ([^{18}F]FDG) and sodium [^{18}F]fluoride ([^{18}F]NaF) for inflammation and calcification, respectively.[49,51] However, the existing limitation with [^{18}F]FDG is that while it is capable of targeting inflammatory biomarkers associated with AS preceding CAVD, it is incapable of assessing its severity.[51] On the other hand, in a study by Hyafil et al., they demonstrated that [^{18}F]NaF showed high uptake in valvular calcifications of patients presenting with aortic stenosis and that their methods were highly reproduceable.[52] Furthermore, in comparison to [^{18}F]FDG, [^{18}F]NaF was shown to be a superior indicator of disease progression.[51,52] Following improvements in hybrid nuclear imaging systems, the feasibility of using PET for imaging small structures has increased

drastically. Despite the greater specificity of [^{18}F]NaF over [^{18}F]FDG in early valve disease detection, it still faces shortcomings such as spill-over effects (in this case from adjacent bones) and poor resolution in smaller structures.[50] While it remains to be a key diagnostic tool for imaging valve insufficiencies resulting from advanced atherosclerotic plaques or calcification, this late stage disease detection and monitoring calls for imaging agents at earlier timepoints in disease progression.

As for newer imaging markers of interest, one attractive target is the various MMPs, specifically -1, -2, -9, -12 and -13 which are upregulated in CAVD.[15,53] Contrasting well established clinical tracers, a newly available radiotracer used for detecting MMPs has shown promising results in assessing progression of CAVD in mice. [^{99m}Tc]RP805 is a pan-MMP radiotracer developed by Sadeghi et al. and shows increased uptake in the aortic valve region in CAVD positive mice.[3] This radiotracer shows high specificity for its target and makes use of the paired SPECT/CT hybrid imaging system.[3] The added benefit of CT allows for anatomical reference in the scan, superior to a transmission scan needed for reconstruction in non-hybrid imaging systems. Contrasting this work, in terms of what is being synthesized in the lab, two new radiotracers which are available for PET imaging, a system with improved resolution over SPECT, are being used to assess MMP expression. The first is [^{18}F]FMBP, a radiotracer with target specificity for MMP-13 (a proxy for MMP-1 imaging in mice) and the second is [^{18}F]BR351, a pan-MMP radiotracer with increased affinity for MMP-2 and -9 (Figure 2). These in-lab synthesized radiotracers will play a critical role in detecting progression of CAVD as MMP expression has shown to be upregulated at early timepoints of disease progression.[3,54] This contrasts the clinically evaluated radiotracers which tend to only detect targets of interest in advanced disease

states where management may no longer be feasible and interventions will be aimed more at invasive treatment options such as surgery instead of prevention.

Whilst the exact mechanism by which these radiotracers work is beyond the scope of this thesis and mentioned elsewhere, briefly, [^{18}F]FMBP shows selectivity for MMP-13 as it binds to a series of amino acids that make up the S1 and S1' domain, a specificity pocket adjacent to the catalytic site.[55] As for [^{18}F]BR351, this radiotracer binds to the catalytic zinc domain, conserved across MMPs, thereby reducing its selectivity for individual isozymes. That being said, based on selectivity data from previous studies, BR351 is most potent for MMP-2 and -9 and is therefore classified as having selcetivity for these gelatinases as opposed to other MMPs which it may also be binding to a lesser degree.[55,56]

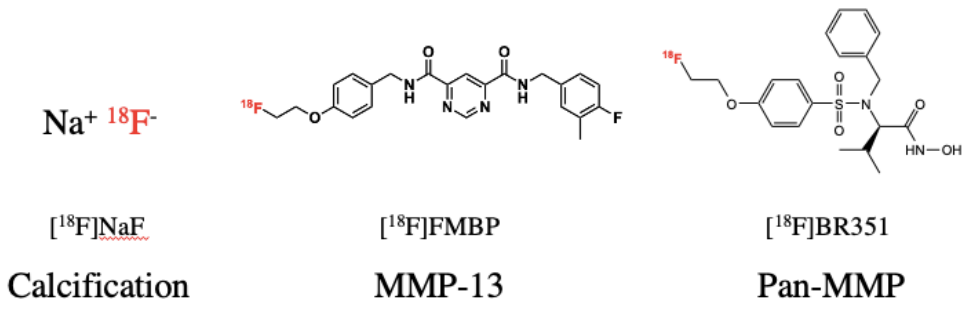

Figure 2: Radiotracers for PET and Autoradiography Studies
Chemical structures of [^{18}F]NaF, [^{18}F]FMBP, and [^{18}F]BR351 used in PET and autoradiography studies. [^{18}F]NaF is taken up by bone after binding to hydroxyapatite coordinated by calcium ions. [^{18}F]FMBP and [^{18}F]BR351 are taken up by tissue (such as atherosclerotic plaques within the aortic sinus) expressing MMPs during active remodelling of the extra cellular matrix following tissue response to injury.

1.8 Histochemical and Immunohistochemical Staining

Aside from *in-vivo* imaging, an important part in the characterization of predictive CAVD biomarkers are those which are obtained through histological, ex-vivo analysis. Referenced in the literature, typically expressed CAVD biomarkers which can be further

visualized and quantified include but are not limited to; leaflet calcification, macrophage expression, MMP-2, -9, and -13, (localization and activity), formation of atherosclerotic lesions, and degraded collagen in ECM remodelling.

1.9 Hypothesis and Objectives

1.9.1 Hypothesis

Due to the expression and upregulation of MMP-2, -9, and -13 in a murine model of CAVD, targeted molecular imaging of these biomarkers with high specificity serves as a sufficient indicator of disease progression at earlier timepoints than are offered by current clinical standards of care.

1.9.2 Molecular Targets and Imaging Probes

The first goal of this study is to characterize potential molecular targets in rodent models and human tissue specimen. Furthermore, we want to be able to evaluate experimental molecular imaging probes to predict CAVD progression. Lastly, within this sphere, we want to corelate expression of histologically identified biomarkers to PET radiotracer binding and expression.

1.9.3 Valve Morphology Characterization

The next goal of this study is to determine the feasibility of characterizing valve leaflet morphology in mice as either BAV or TAV by 2D B-mode planar echocardiography. Currently, valve morphology in research studies with mouse models is characterized post-mortem via histological tissue preparation. Analysis by *in vivo* imaging

will allow for longitudinal studies with smaller sample sizes as animals can be assessed at various timepoints for disease progression.

1.9.4 Valve Area

Continuing on the previous objective, our next goal is to be able to assess the area of the valve opening as it is an important diagnostic factor in AS preceding CAVD. As is seen in the clinic, we want to assess valve area by echocardiography analysis and by making use of the continuity equation as opposed to 2D B-mode planar imaging (Appendices A and B).

1.9.5 Human Valve Tissue Histology and Autoradiography

Our next goal involves the use of acquired human tissue samples from patients with varying degrees of CAVD progression. The use of human valve tissue for immunofluorescent, immunohistochemical (IHC) staining, and autoradiography can serve as an indicator of relative biomarker expression and the comparability between animal models. Supplementation of human tissue data to the study would provide an additional component lacking in the existing literature of the field with respect to novel imaging probes for early detection of CAVD biomarkers.

1.9.6 Radiotracer validation for assessing progression of CAVD

Lastly, we would also like to be able to determine radiotracer uptake and binding to biomarkers of interest through a variety of molecular imaging modalities including; *in vivo* and *ex vivo* PET as well as *in vitro* and *ex vivo* autoradiography.

2.0 Methods

2.1 Animal Models and Experimental Design

Male and female ApoE$^{-/-}$ (B6.129P2-*ApoE*$^{tmL/Unc}$/J, strain no. 002052) and WT C57Bl/6 J (strain no. 000664) mice were obtained from Jackson Laboratory. Experimental animals were started on a western diet (TD.88137, Envigo) at 4 weeks of age while WT remained on normal rodent chow (Figure 3). The diet is composed of 42% of total calories from fat, making up 21.2% of the weight and 0.2% cholesterol. Animals which were originally started on 0.25% cholesterol diets developed skin lesions and did not survive long-term. Animals being aged past the 4-month timepoint were taken off of the western diet after approximately 4 months and returned to normal chow until either the 8-month or 12-month study timepoints, respectively. Both strains were given unrestricted access to food and water. In the event of skin lesion formation, animals were treated with a topical ointment supplied by Animal Care and Veterinary Staff (ACVS) and were additionally treated with saline by subcutaneous injection when showing signs of dehydration. Any animals which experienced adverse effects as a result of diet or other outstanding factors not accounted for in this study were removed to ensure animal ethics were maintained and that confounding variables were not introduced to the study design. All husbandry, care, and experimental protocols were approved and carried out with adherence to the guidelines outlined by the Canadian Council on Animal Care, the ACVS team at the University of Ottawa Heart Institute, and the University of Ottawa Animal Care Committee.

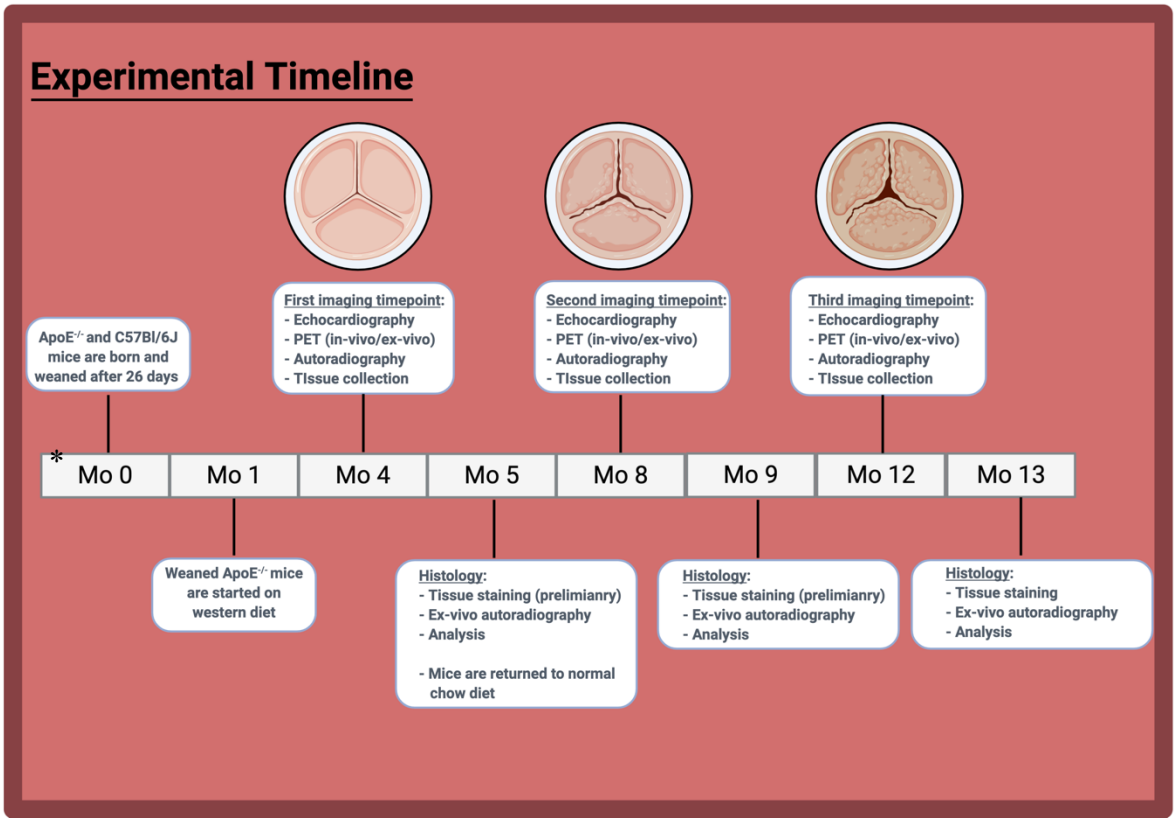

Figure 3: Experimental Timeline
Layout of experimental timeline outlining key timepoints integral to the study design. After the mice needed for this study were born, they were housed with their litter and then weaned after 26 days post-gestation. At this point, animals were now 1-month old and could be transferred from feeding off their mothers and separated to be housed with animals of the same sex and, for the ApoE$^{-/-}$ model, can be transferred to the western diet as mentioned previously. After three months on this diet intended to advance atherosclerosis (now 4 months of age), animals have arrived at their first imaging timepoint consisting of echocardiography, PET, and tissue collection for histological analysis in the following weeks. These same studies were then repeated at 8 and 12 months, respectively. Note that after 4 months of western diet, animals were returned to normal chow to stop the rapid acceleration of disease pathogenesis. Illustrations of disease progression are outlined over the 4, 8, and 12 month timepoints to identify expected disease progression from normal healthy valve architecture, through aortic sclerosis, and finally to advanced CAVD. *Mo = months. Made with Biorender©.

2.2 Radiotracers

All precursors and radioactive compounds were synthesized by other lab members as part of an ongoing atherosclerosis project in addition to this ongoing study. Given that the chemical synthesis is beyond the scope of this thesis it has been omitted. Radioactivity for

labelling compounds was produced on site by the core radiochemistry lab's in-house cyclotron.

The radiotracers produced on site are [^{18}F]BR351, [^{18}F]FMBP, and [^{18}F]NaF which were used for imaging the uptake of MMP-2/-9, -13, and bone/calcium respectively (Figure 2). The same tracers were subsequently used for *ex-vivo* PET and *in vitro* autoradiography. Fluorine based radiotracers were selected due to ^{18}F having a half-life of 109.7 minutes (approximately 2 hours), making it suitable for imaging, autoradiography, and biodistribution studies.

2.3 Echocardiography

Animals were imaged using a Vevo3100® imaging system (VisualSonics©) with a 550 Hz and 400 Hz transducer. Animals were placed under light isoflurane anesthetic (1.5%) and their limbs secured down with tape to keep them in a supine position. This way their heart rate (maintained between 450-600 bpm) could be monitored by built-in ECG pads lubricated with conductive gel and temperature was monitored via a rectal thermometer (held between 32-38 °C) to ensure physiological conditions were maintained. In unique circumstances where size limited the ability to fix the limbs to the heating pad, ECG probes were inserted subcutaneously using provided gating needles. To ensure even and consistent heat to monitor animal temperature, an additional heating lamp was placed adjacent to the imaging platform and used as needed. To improve resolution, a generous amount of water-based ultrasound gel was applied to the imaging site.

Prior to imaging, the animals were anesthetized using isoflurane (3-4%) and their abdominal and thoracic regions were shaved bare to allow for better transducer contact and

access to the acoustic window to enhance image resolution. Hair was removed first by using an electric shaver (Philips©) followed by hair removal cream (Nair^{TM}). After one minute, the cream was removed using warm water and a cotton swab.

Each mouse (WT and ApoE$^{-/-}$ $N \geq 7$ mice per cohort) underwent the same imaging procedures starting with a parasternal long-axis view (PLAX) and paired EKV to determine left ventricular outflow tract (LVOT) diameter (Appendix B – Figure 16). When possible, the imaging window was decreased and focal point adjusted to ensure that the frame rate of the imaging system could be improved (shortening scan times) and that the area being imaged was in optimal view, respectively. Supine animals were tilted up and to the left to ensure the heart was brought forward and leftward, closer to the chest wall to ensure a superior acoustic window with minimal shadowing from surrounding ribs and sternal structures. This was followed by a parasternal short axis (PSAX) and M-mode view and tracing (Appendix B – Figure 17). LVOT diameter was measured just inferior to the cusps of the aortic valve in the PLAX to ensure reproducibility between groups. It was measured from the white–black interface of the septal endocardium to the anterior mitral leaflet with the acquisition parallel to the aortic valve plane. Following this measurement, peak velocity, mean gradient and velocity time integral (VTI) were measured in PLAX with pulse wave and colour doppler taken at either end of the aortic valve in the region of fastest blood flow as denoted by the provided false colour table adjacent to the scanning window (appendix B – Figure 18). The colour doppler window was sized to appropriately image the region of interest (ROI). In addition, a consistent gate width of 0.47 mm and measurement angle (53° +/- 5°) parallel to blood flow were maintained to avoid over or underestimating quantitative measurements. The angle of the recorded measurement never

surpassed 60° as anything over this value cannot be quantified accurately using the associated imaging software.

The metrics obtained further allow for analysis and calculation of AVA, assessment of stenosis (peak velocity <1600 mm/s)[1], and differences in pressure across the AV (measured as mean gradient) in VisualSonics® analysis software (Appendix A – Figure 15). Lastly, valve morphology was assessed in the PSAX view by sliding the transducer rostrally from the level of the papillary muscles (Appendix B – Figures 19 and 20).

All data was acquired through the Vevo3100® built-in image acquisition workstation and analyzed through the associated software provided by VisualSonics®. In the software, LVOT is measured using a linear measurement tool while all other metrics are analyzed by tracing the peaks generated by the pulse-wave doppler scan. Brightness and contrast are adjusted to ensure the full peak is captured and tracing points are adjusted after the fact to correct any user tracing error. Measurement angle is also checked to ensure the theta value is the same at the level of LVOT and valve between measurements within the same animal.

2.4 Histology

All instrumentation relating to sectioning were obtained from Leica® unless otherwise stated. Serial sections were obtained starting at the aortic root all the way through the aortic annulus. Embedded tissue is sectioned from frozen block tissue samples using a cryostat at 10 μm for staining and *in situ* zymography and 20 μm for autoradiography. Tissue sections were collected on glass slides (Fisherbrand™ SuperFrost™Plus Microscope Slides) and left to air dry for 30 minutes prior to storage at -20 °C.

Paraffin embedded tissue was sectioned on a microtome at 5 μm for staining and immunohistochemistry. Sections were collected from a 45 °C water bath and mounted on glass slides and then left to cure in a 40 °C oven overnight and then stored at room temperature.

2.5 Staining, Immunohistochemistry, *In Situ* Zymography

All reagents used for staining were provided by Sigma Aldrich unless otherwise specified. This study aimed to identify a wide series of molecular and biological markers indicative of disease progression. For the following staining, general procedural guidelines were followed as conventionally reported. This includes; hematoxylin and eosin for leaflet thickness and preliminary tissue evaluation, picrosirius red (PSR) for collagen remodelling, oil red-O (ORO) for lesion lipid content, and alizarin red for microcalcification in lesions and valve leaflets. For quantification, all samples were compared relative to other timepoints as well as to their age-matched control tissue. Leaflet thickness and lesion size were measured as a percentage of sinus area and calcification was measured as percent positive area in the leaflet and lesion areas respectively.

For immunohistochemistry, all antibodies were obtained from Abcam. Tissue sections were deparaffinized following standard deparaffinization procedures and then transferred to a water bath (pH 7.0). Antigen retrieval was then performed in citrate buffer (pH 6.0) at 100 °C for 150 seconds and then rinsed with distilled water (1 x 5 min) and 1 x PBS (2 x 5 min). Sections were covered in 10% normal goat serum (Vector Laboratories®) for 10 minutes and incubated with a combination of either 1:100 rabbit polyclonal MMP-13 (ab39012), 1:200 rabbit polyclonal MMP-2 (ab97779, or 1:200 rabbit polyclonal MMP-

9 (ab38898) primary antibody and 1:500 mouse/human monoclonal Mac-2 primary antibody (CL8942AP) for approximately 16 hours at 4 °C. After washing with phosphate-buffered saline (PBS) (2 x 5 min), samples were incubated with a combined secondary antibody comprised of 1:500 goat anti-rabbit for MMPs (Invitrogen®) and 1:500 goat anti-rat for MAC-2 (Invitrogen®) for 30 minutes. Nuclei were counterstained with Hoeschst 33258 (10 mg/mL in 1x PBS) for 8 minutes and washed with 1x PBS (2 x 5 min). Slides were mounted with fluorescent protective mounting media (Dako), and cover-slipped, dried, and stored in dark at room temperature until imaging by fluorescent microscopy (Leica® Slide Scanner®).

In situ zymography was performed using a SensoLyte ® 520 Generic MMP Activity Kit (Anaspec®) on 10 μm fresh tissue. After allowing tissue to air dry for approximately 30 minutes, tissue was rinsed in a water bath (3x) to remove OCT and then heated to 37 °C along with all working solutions. Tissue was first incubated in a 1 mM 1:1000 AMPA:buffer solution for 40 minutes and then covered with a 1:100 substrate:buffer solution for 1 hour. Tissue samples were then washed in distilled water (2x) and mounted with 30% glycerol in PBS and a cover slip. Imaging of activated MMPs was completed using a fluorescent microscope (Zeiss) and Leica® Slide Scanner®).

Images were acquired with Aperio ImageScope software and quantified through ImageJ software. For brightfield analysis, images were first screen captured in Aperio ImageScope and a global scale bar of 900 μm was set for all images acquired. Then, in ImageJ after the first scale bar had been set (this remained constant for all figures), first an ROI was drawn around the sinus followed by ROIs for each lesion within the leaflets present. For leaflet area, this was used as a proxy for leaflet thickness and an ROI was first

drawn around the sinus and then ROIs were drawn around each leaflet. The area measurements generated in ImageJ were then graphed using GraphPad Prism 7.0 (GraphPad Software, Inc.). For measurements of biomarker percentage within a region, a sinus area ROI was first recorded followed by ROIs being drawn around each tissue structure where the biomarker was present and saved with their area recorded. Next, under "image" → "adjust" → "colour threshold", hue, saturation, and brightness were adjusted depending on the stain used (*e.g.*, ORO or Alizarin Red) and kept constant across all samples to ensure consistency. For ORO, the minimum hue value was set to 185 and the max at 244, saturation was set to a minimum of 35 and maximum of 255, and for brightness, the minimum was set to 0 and the max was set to 255. For alizarin red the same parameters were used but for hue, the minimum was set to 184 and the maximum to 249. Once completed, the image was converted to 8-bit, thereby converting the image to greyscale and then a threshold was applied dependent again on the stain being used. For ORO the threshold was set to a minimum of 0 and a max of 122. For alizarin red the threshold was set to a minimum of 0 and a max of 115. Lastly, the recorded tissue specific ROI was brought up and the threshold values recorded in order to calculate stain percentage per biomarker of interest.

For immunofluorescence, similar procedures were followed but first merged images were separated into their respective colour channels. From here, a false colour balance adjustment panel was used to draw ROIs against the dark background and then similar steps were carried out to determine the percentage of Mac-2, MMP-2, -9, and -13 in ROIs. Alternatively, if there had been a lot of background noise present, relative fluorescent intensity could be calculated via similar methods as were previously mentioned with the

addition of an averaged background ROI which could then be subtracted from obtained relative fluorescent intensity.

2.6 Positron Emission Tomography

PET imaging was conducted using a D-PET (Siemens) small animal imaging system. Animals were placed under light isoflurane anesthetic (2%) in O_2 and imaged through a dynamic scan over a period of 60 minutes. During *in vivo* scans animals were kept warm by using a heat lamp placed adjacent to the camera to ensure the maintenance of physiological conditions. Prior to initiating the scan, a 10-minute transmission scan was acquired for image reconstruction purposes. Images were reconstructed through 3D OSEM MAP programmed into the Inveon Acquisition Workplace (IAW). Regular instrument calibration and quality control using on-site germanium rod sources ensured accurate image acquisition and reconstruction.

For all PET studies, animals were dosed with approximately 10 μCi/g of radiolabelled compound and tracer was administered intravenously through a tail-vein catheter. Prior to catheterization, the animals' tails were cleaned and sterilized with an alcohol wipe (Loris^{TM}) and once inserted, catheters were flushed with a 0.9% saline solution containing 10% heparin. Catheters were constructed using 27G (BD) needles and PE10 tubing fitted with a 1 mL syringe (BD). Upon removal of the catheter, silver nitrate tipped rods were used to cauterize any blood. After imaging, animals were returned to their respective cages and monitored until recovery.

For *ex vivo* PET studies, similar experimental protocols and conditions were carried out with the difference being that animal euthanasia took place prior to scanning (Section

3.5). Harvested hearts and aortae were placed in stacked petri dishes (Fisher©) and imaged during a static scan of 30 minutes 1-hour post tracer administration.

Images were reconstructed using built in IAW software where necessary data corrections can be made such as; random and scatter coincidence events, dead time correction, and decay to name a few. Images were then post-processed using Amide© software with further data processing and quantification in Microsoft Excel®.

In Amide, reconstructed scans were viewed in the transverse, coronal, and sagittal planes where accurate ROIs could be drawn around various organs of interest for construction of time activity curves (TAC). Time gating could be established to monitor uptake over the scan and produce a clear picture of various organs. Furthermore, the minimum and maximum intensity values could be adjusted to help distinguish structures from the background and colour assignment was achieved by selecting a scheme with an associated colour lookup table. The injected dose per animal could also be inputted and accounted for using this software. Once 3D ROIs were drawn, the software could calculate the ROI statistics accounting for removal of background noise produced during the scan by poor transmission scan reconstruction or animal movement. The processed data could then be exported to excel where the injected dose (measured in nCi/cc) could be calculated and TACs generated in units normalized for injected dose (%ID/cc).

2.7 Tissue Collection and Sample Preparation

Following imaging, tissue was harvested for sectioning and subsequent analysis. Animals were anesthetized using isoflurane gas (3%) and then sacrificed by cardiac perfusion. A 1 mL needle was inserted into the left ventricle and blood was removed from

the circulation. Using fine tissue surgical scissors (FST), an incision was made in the right atrium to reduce pressure during perfusion. Then, 15 mL of 1x PBS was flushed through the vasculature to ensure full perfusion. Tissue was then removed until the heart and aorta were visible. With the animal supine, a blunt incision was made superior to the thymus to separate the branching carotids and respiratory tract. Using forceps to grip the apex of the heart, a series of cuts were made below the aorta along the spine caudally. The aorta was then detached at the aortic bifurcation (approximately the level of the fourth lumbar spine).

Under a dissection microscope (Krüss Stereomicroscope – MSL4000-series), adventitia was removed from the aorta and was detached superiorly from the heart. With the heart isolated, a cut was made along the short axis below the level of the atria.

The remaining tissue, which contains the aortic valve was then embedded in either paraffin or Optimal Cutting Temperature (OCT) media (Fisher®). If embedding tissue unfixed, it was first frozen in a mould (Fisher©) filled with OCT on a metal block in liquid nitrogen and then stored in aluminum foil at -20 °C until processing or -80 °C long term. Tissue embedded in paraffin was first fixed by storing for 48 hours in 10% formalin (Fisher®) before being processed by the core histology lab. Following processing, the tissue was embedded in paraffin wax (TissuePrep®) and stored at room temperature until sectioned.

2.8 Human Tissue Collection and Analysis

Human aortic valve specimens with normal pathology obtained from heart transplant recipients and moderate to severe AS valves obtained at the time of surgery were used to confirm the presence of biomarkers present in animal models. Co-localization of molecular

imaging targets with calcification and inflammation are assessed and specific binding of each radiotracer is compared across groups of valves. Positive tissue is collected from patients undergoing valve replacement surgery whilst controls are obtained from patients undergoing heart transplants and other donors. Tissue is harvested fresh and transported in ice cold 1x PBS (approx. 4 °C). Tissue is then embedded in OCT embedding media for preparation of cryostat sectioning. Tissue is stored at -20 °C short term and -80 °C long term (>1 month). All ethics and protocols have been approved by the Ottawa Health Science Network Research Ethics Board (OHSN-REB), the University of Ottawa Heart Institute, and the University of Ottawa Office of Research Ethics and Integrity.

2.9 Autoradiography

In vitro autoradiography was performed on fresh tissue samples previously embedded in OCT. Sections were cut at 20 μm, air dried for 30 minutes, and then washed to remove embedding media. Samples were then divided into baseline and block water baths and incubated with aforementioned radiotracers (1 μCi/mL) for 1 hour. The blocking solution was comprised of using excess nonradioactive standard (2 μM) and the same concentration of activity as in the baseline study. Post-incubation, samples were rinsed in separate baths of 1x PBS (3 x 5 min) and then left to air dry. The slides were then immediately exposed to a super-resolution Storage Phosphor Screen (BAS-IP SR 2025 E) in an Electrophoresis Systems Autoradiography Cassette (FBXC 810) overnight. The phosphor screen was scanned with a Cyclone Plus Storage Phosphor System and images were analyzed using OptiQuant software. By drawing ROIs around tissue samples, relative light units (RLU) were calculated and then converted to units of activity by using a set of

calibrated standard curves with decay corrected activities (Appendix D – Figures 22 and 23) and measured on the same screen. Activity density (counts/mm^2) was calculated from dividing the sample activity by the area of the ROI. Alternatively, ROI intensity was measured using ImageJ software as previously described (section 2.7).

2.10 Statistical Analysis

Data are presented as the mean +/- SE. Group comparisons were done using a 2-tailed Student t test (for equal variances) or paired t test (for paired samples). Multi-group comparisons were done using 2-way ANOVA with Tukey's multiple comparison test. Confidence intervals were set at 95%. Statistical analysis was performed using GraphPad Prism 7.0 (GraphPad Software, Inc.). Data was analyzed for outliers using ROUTs test with a Q variable set at 1% to balance the likelihood of definitive and likely outliers.

3.0 Results

3.1 Echocardiography

Experimental CAVD and WT animals (Section 2.1) were evaluated by echocardiography at three distinct timepoints (4, 8, and 12 months) for hemodynamic assessment of CAVD progression. The experimental group was composed of ApoE$^{-/-}$ mice fed a western diet for 3-4 months (depending on timepoint evaluation) in order to advance disease severity as previously described. Imaging via echocardiography consisted of obtaining relevant metrics predictive of AS, an important feature preceding CAVD progression as previously outlined in clinical and other animal studies.[57,58] This included the assessment of peak velocity, mean pressure gradient, aortic valve area, and valve morphology.

The ApoE$^{-/-}$ group showed increased peak velocity indicative of stenosis (peak velocity >1600 mm/s) after 8-months in comparison to WT, 2161.65 mm/s ± 112.28 mm/s vs. 1237.87 ± 84.90 ($p < 0.00001$) and again at 12 months 1785.82 mm/s ± 102.45 vs 1729.93 mm/s ± 365.23 ($p = 0.0057$) at the level of the AV (Figure 4,A). There was no observed difference, however, at baseline evaluation (4 months) between the ApoE$^{-/-}$ and WT groups. The same holds true for baseline evaluation of mean gradient. Like peak velocity, mean gradient also increased significantly at 8 months between groups in ApoE$^{-/-}$ animals versus WT at the level of AV, 7.45 mmHg ± 0.92 vs 2.42 mmHg ± 0.31 ($p<0.00001$) (Figure 4,B). There was no observed difference between groups at the 12 month timepoint, however.

For AVA, there was a significant decrease in experimental animals from 8 to 12 months, 0.75 mm^2 ± 0.07 vs 1.33 mm^2 ± 0.07 ($p<0.0001$) and AVA also decreased significantly at 12 months between ApoE$^{-/-}$and WT animals, 0.75 mm^2 ± 0.07 vs 1.31 mm^2 ± 0.08 ($p<0.0001$) (Figure 4,C). No difference in AVA was noted at baseline measurement between groups. Interestingly, there was also a significant decrease in AVA from 4 to 8 months, 1.84 mm ± 0.06 vs 1.41 mm^2 ± 0.11 ($p<0.0071$) in WT animals. There was no change, however, in the WT group from 8 to 12 months indicating that it is likely that healthy animals do not progress to the disease state with age being the sole contributing variable. These findings are in accordance with changes observed in peak velocity as while some WT animals did display peak velocities above 1600 mm/s, none of them developed severe AS in comparison to the experimental ApoE$^{-/-}$ group which presented with peak velocities in the realm of >2000 mm/s in some instances. It is important to note that in some cases, animals developed peak velocities around 4000 mm/s but these findings were

consistent with displayed aortic regurgitation (AR), a vastly different disease from AS. This is suggestive of the animal model developing what is referred to clinically as mixed disease (section 4). Furthermore, findings are in accordance with the literature which indicates that mice only develop hemodynamically significant AS between approximately 9-12 months of age if at all.[15]

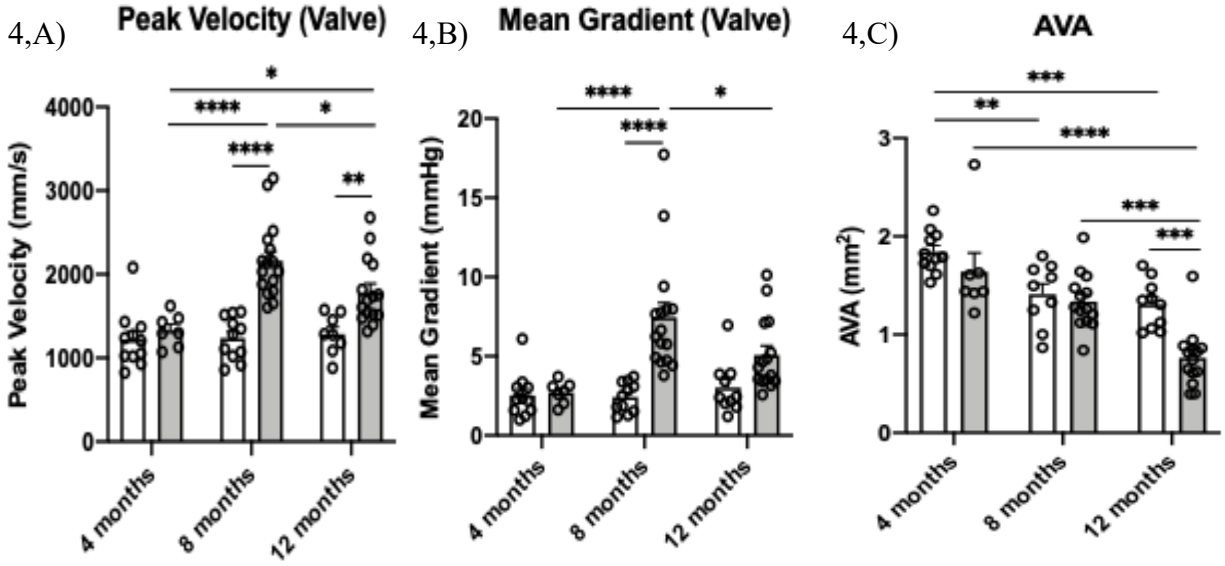

Figure 4: Progression of AS leading to hemodynamically significant CAVD
Echocardiography analysis in ApoE$^{-/-}$ vs WT animals at 4, 8, and 12 month timepoints. Peak velocity at the level of the valve >1600 mm/s indicates hemodynamically significant disease progression in mice. ApoE$^{-/-}$ Show significantly higher peak velocity at the 8 and 12 month timepoints ($p < 0.0001$ and $p = 0.0057$, respectively). (**A**). Mean gradient indicated features of AS with significantly increased pressure at 8 months in ApoE$^{-/-}$ mice in comparison to WT ($p < 0.0001$) (**B**). Lastly, decrease in aortic valve area (AVA) is calculated using the continuity equation (Appendix A – Figure 15) and serves as an indicator of stenosis in mice. ApoE$^{-/-}$ mice present with significantly decreased AVA in comparison to WT animals at 12 months ($p = 0.0071$) (**C**).

3.2 Histology

Following tissue collection, a series of stains were carried out for preliminary assessment of disease progression and presence of biomarkers of interest. Hematoxylin and

eosin staining was completed to determine tissue morphology (Figure 5,A). Additionally, it allowed for quantification of leaflet area in WT vs ApoE$^{-/-}$ tissue as well as at the three different timepoints. Leaflet area as a percentage of sinus area in intended to serve as a proxy to leaflet thickness.[1] It is important to note that leaflet thickening was not observed in WT animals at any of the three timepoints (Appendix C – Figure 21) but increased proportionally with age in the ApoE$^{-/-}$ group (Figure 6).

As expected, there was also an observed increase in lesion area in comparison between WT and ApoE$^{-/-}$ mice as made evident from staining for lipids with ORO (Figure 5,B). The WT group did not develop any lesions within the aortic sinus at any of the three timepoints (Appendix C – Figure 21). Furthermore, there was an evident increased lesion area within the experimental ApoE$^{-/-}$ group at different timepoints with increases tapering off over the 8 and 12-month timepoints (Figure 6). Lesion area was calculated as a percentage of aortic sinus area. Interestingly, percentage of ORO (the amount of staining within the lesion itself) decreased within the ApoE$^{-/-}$ group proportionately to age. It is difficult to say with certainty that this trend will continue given the small sample size but one plausible explanation for this observation is due to lesion area increasing with age while the plaque contents change. Over time, the formation of calcified nodules or the development of a necrotic core will account for a substantial portion of the lesion area, thereby effectively decreasing the amount of ORO able to bind lipids within that region.

Next, calcification was assessed using alizarin red and it was shown to be only present in the 8 and 12 month ApoE$^{-/-}$ groups (figure 5,C). No calcification was noted at the 4-month timepoint or in any of the WT animals (Appendix C – Figure 21). Again, due to the small sample size, it is challenging to draw any definitive conclusions at this point.

Similar results to lesion calcification were observed within the leaflets of the ApoE$^{-/-}$ model. Visually, calcification seemed to be fairly dispersed within the lesions of the aortic sinus whereas it was predominantly localized to the hinge region of the leaflets where they intersect with the lamina of the aortic sinus. Further analysis is required to draw more concrete conclusions.

Lastly, PSR staining was performed to assess the presence of collagen remodelling in both the lesion and leaflets of the AV (Figure 5,D). Collagen remodelling, however, is absent in WT animals (Appendix C – Figure 21). As is the case with some of the other stains, more tissue needs to be analyzed to differentiate the degree of matrix remodelling. In addition, once the tissue has been stained, imaging can be completed under polarized light to differentiate between collagen types within the lesions and leaflets of the valve.

For immunohistochemistry, the first staining with Mac-2 for macrophage deposits suggests an increase in inflammatory response in more progressed disease state animals (Figure 7). Macrophage accumulation was evident in the lesions of aortic sinus sections suggesting inflammatory marker migration as disease progression continues and a necrotic core is formed within the endothelial lesions. MMP-2, -9, and -13 expression was also assessed and it was found that there was a relative increase in MMP-2, and -9 but not -13 expression in diseased animals after preliminary assessment (Figure 8). As predicted, MMP expression showed to localize to macrophage expression and was absent in WT animals. Further analysis is required to determine exact expression levels of each MMP at the various timepoints.

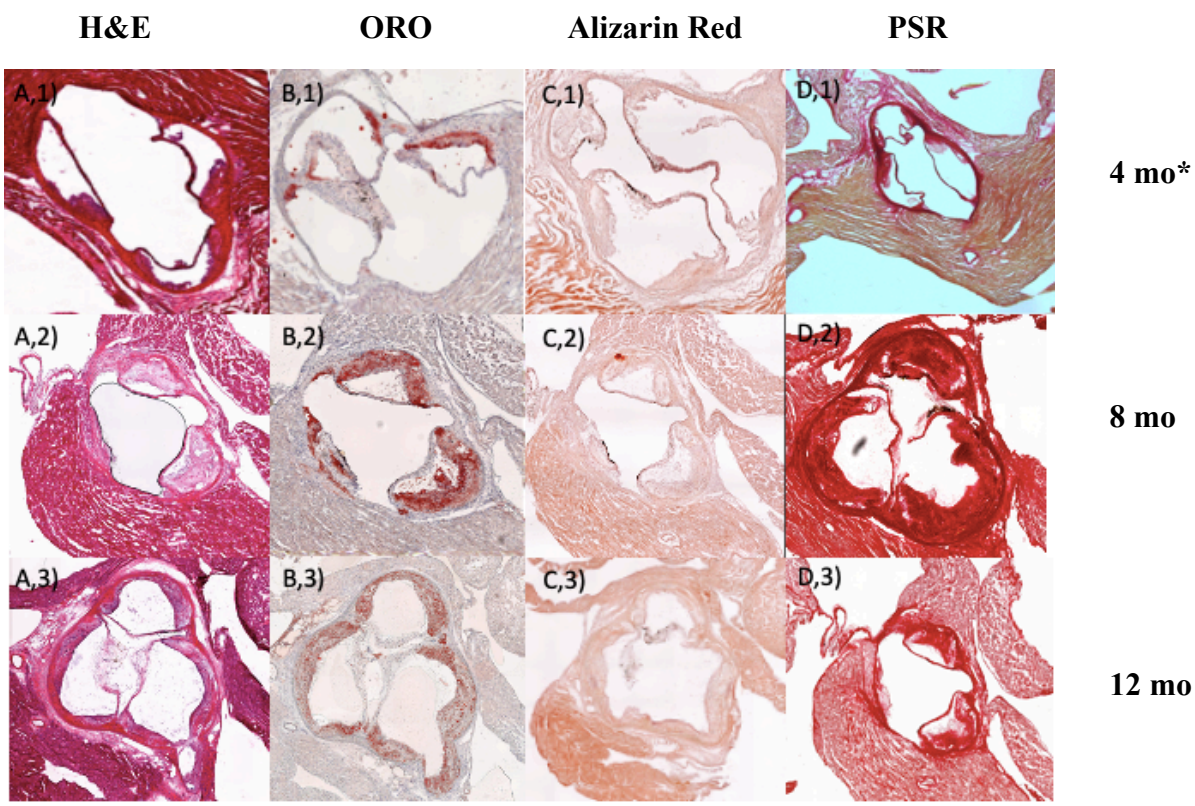

Figure 5: Histological Analysis of Various Biomarkers of Interest in ApoE$^{-/-}$ mice
Representative histological panel indicating various biomarkers which are upregulated in the progression of CAVD. WT animals do not express quantitative measures of disease progression (Appendix C – Figure 21). Moving top to bottom represents the expression of each biomarker at either 4, 8, or 12 months, respectively. In the first panel, a representative figure of hematoxylin and eosin indicates changes in tissue morphology and leaflet thickness (**A,**). ORO indicates lipid staining within various atherosclerotic lesions which form within the aortic sinus (**B**). Alizarin red is used for the detection of microcalcifications within the lesion and leaflets, respectively (**C**). Picrosirius red is used for representation of collagen remodelling within the lesion of the aortic sinus (**D**). All images were acquired using a Leica Slide Scanner and post-processed in Apeiro ImageScope software with analysis in ImageJ. *mo = months

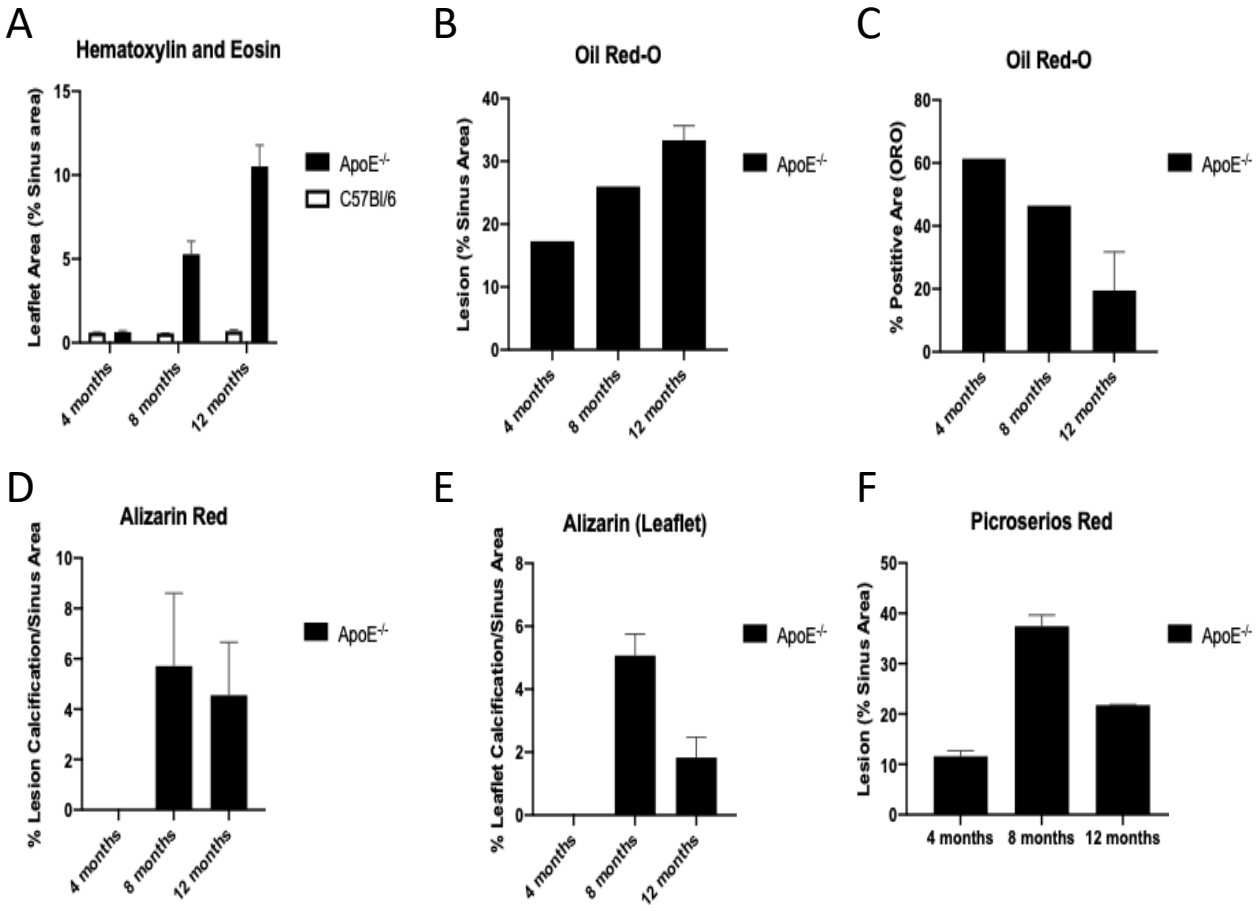

Figure 6: Quantification of various biomarkers of interest
Preliminary evaluation of biomarkers expressed in CAVD progression at 4, 8, and 12 months. Quantification of hematoxylin and eosin indicates percentage of leaflet area within the aortic sinus over time (**A**). Next, lesions as a percentage of aortic sinus area are assessed to monitor the deposit of lipids and degree of matrix remodelling (**B and F**). Following lesion measurement, the percentage of lipid expression and calcification is measured to track how expression changes within the diseased animal model between timepoints (**C-E**).

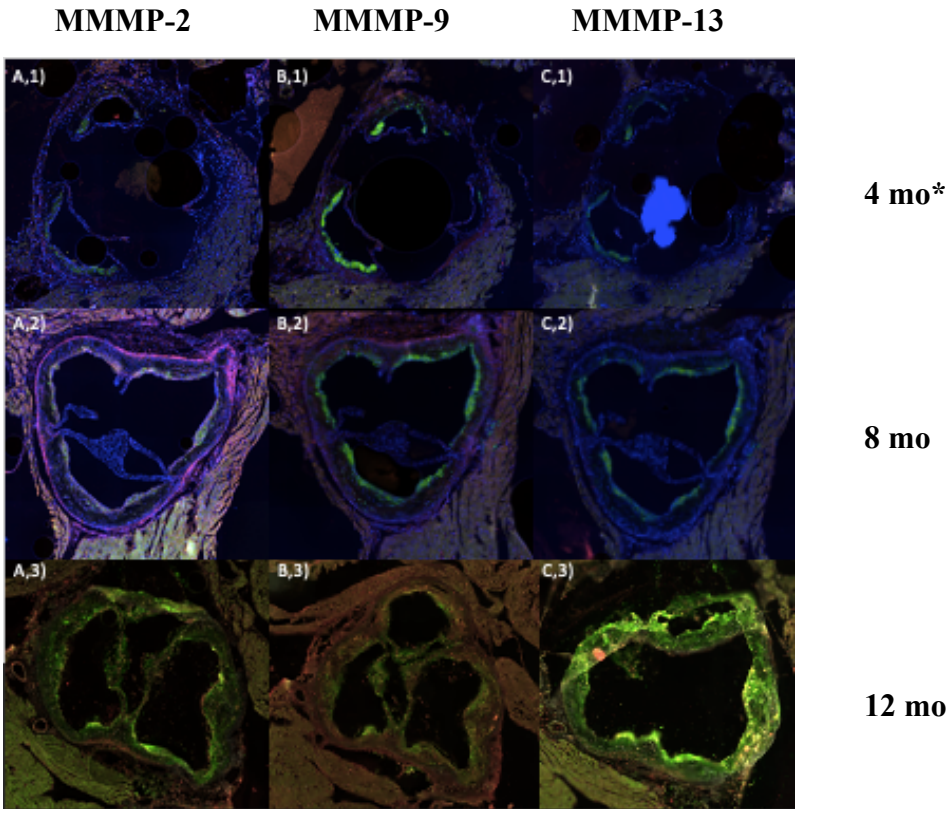

Figure 7: Immunostaining of Various Biomarkers of Interest in ApoE$^{-/-}$ mice
Immunostaining indicates the presence of biomarkers believed to be upregulated in response to CAVD progression. All stains were completed using the same 1:100 concentration of primary antibody in 1 x PBS for MMPs and 1:500 primary antibody for Mac-2 in 1 x PBS. Tissue was counterstained with Hoechst to identify nuclei. Immunofluorescence indicates expression of Mac-2 in green in combination with MMP-2,-9, and -13 in red at the 4, 8, and 12-month timepoints. MMP-2, a gelatinase, is shown to colocalize to Mac-2 expression within the lesion area of the aortic sinus with (**A**). The same holds true for MMP-9, another gelatinase, involved in the matrix remodelling response (**B**). Lastly, staining for MMP-13, a collagenase, is shown across the three timepoints (**C**). Slides were fixed and mounted after staining using Dako to preserve fluorescent intensity for long term slide storage. Images were acquired using a Leica slide scanner and post-processed in Apeiro ImageScope software with analysis in ImageJ. *mo = months.

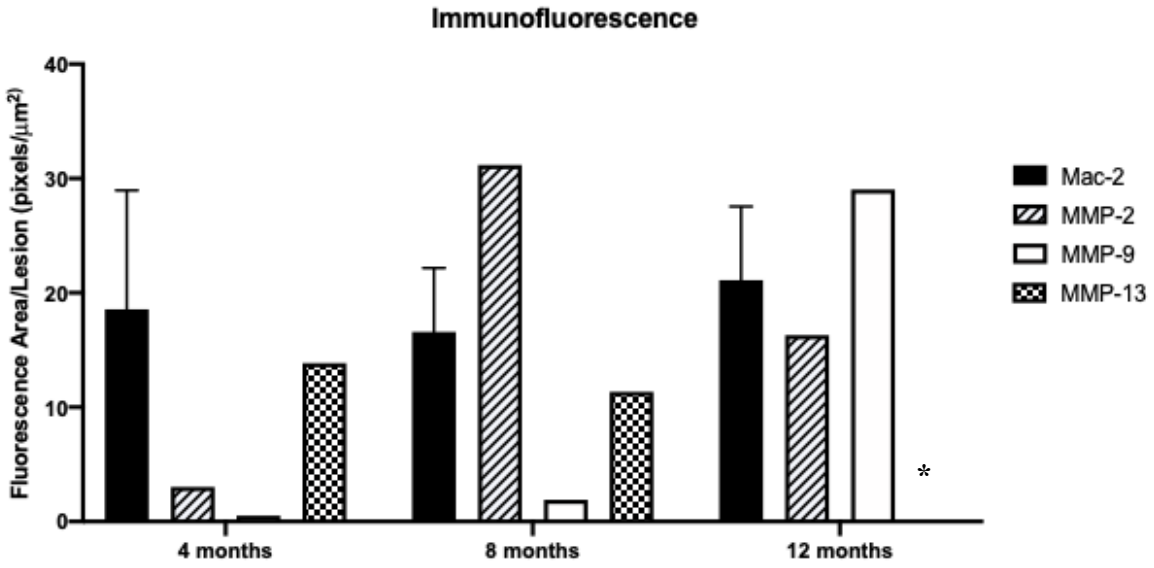

Figure 8: Quantification of Immunofluorescent Inflammatory and MMP Markers Quantification of Mac-2, a immunofluorescent stain for macrophages, in combination with MMP-2,-9, and -13 at the 4, 8, and 12 month timepoints. Images were analyzed using ImageJ software and worked up using Excel and GraphPad Prism. Images exported from Apeiro ImageScope were kept at the same magnification to ensure reproducibility between analyses. *Note that MMP-13 quantification is missing at the 12-month timepoint

3.3 PET Imaging

Three different PET radiotracers were used to assess disease progression and to attempt to visualize biomarkers of interest *in vivo*. For this pilot study, animals were aged to 8 months and were placed on a western diet for 4 months to advance disease progression. Animals were dosed consistently with an injected dose of approximately 10 μCi/g with dynamic scans of 30 minutes for [^{18}F]NaF and 60 minutes for the two MMP tracers. All static scans were done for 30 minutes. Animals were placed under light isoflurane anesthesia (2%) in O_2 and kept warm using a heat lamp for the duration of the scan to replicate physiological conditions. All tracers were administered intravenously through the tail-vein.

Administration of [^{18}F]NaF shows expected uptake into bone after binding to calcium (Figure 9,A). ROIs were then drawn to measure specific uptake per organ as well as blood pool to generate a TAC (Figure 9,B). Once the *in vivo* scan is initiated, the tracer passes through the bloodstream where free $^{18}F^-$ ions bind to calcium in bone whilst the remaining activity is flushed through the excretory system and is taken up in the eliminatory organs (i.e. bladder) as expected. Unfortunately, due to the limited spatial resolution attainable with small animal imaging, it is hard to assess radiotracer uptake in the region of the aortic valve *in vivo.*

Further, with the MMP-13 selective radiotracer, [^{18}F]FMBP, *in vivo* PET studies show similar results to [^{18}F]NaF in that detection of valvular uptake proves challenging and unreliable given the limitations of spatial resolution poised in small animal imaging. That being said, *in vivo* imaging via dynamic PET scan shows tracer uptake over time and routes of elimination after the first pass as expected (Figure 10,A) and provides valuable information when planning to scale up tracer usage for higher order species. Routes of metabolism and elimination seem to be consistent through the liver and intestine, respectively (Figure 10,B). This data is corroborated by additional biodistribution studies which were completed after imaging these animals as part of an ongoing atherosclerosis study in our lab (data not shown).

Given the limitations experienced with the two previous tracers, it was decided to not pursue *in vivo* imaging with [^{18}F]BR351 at this time. Instead, an *ex vivo* PET approach was explored. Interestingly, the activity can be seen binding specifically to plaque regions within the descending aorta and aortic arch as is expected in these regions of increased inflammatory activity with these immuno-responsive cells secreting MMPs (Figure 11,A).

When using [^{18}F]BR351, detection of uptake in the valve area is feasible by *ex vivo* PET but issues with radiotracer binding specificity introduced other confounds resulting in unreliable quantification in these early assessment studies (Figure 11,B). This is largely in part due to ROI's needing to be refined further to better suit the valve area. Given the small structure, it is likely that quantification is impacted by spillover effects caused by using this tracer. Furthermore, it is possible that as the tissue is not perfused, remaining blood containing small amounts of radiotracer remained present and are affecting the quantification by altering the tissue to background ratio (TBR).

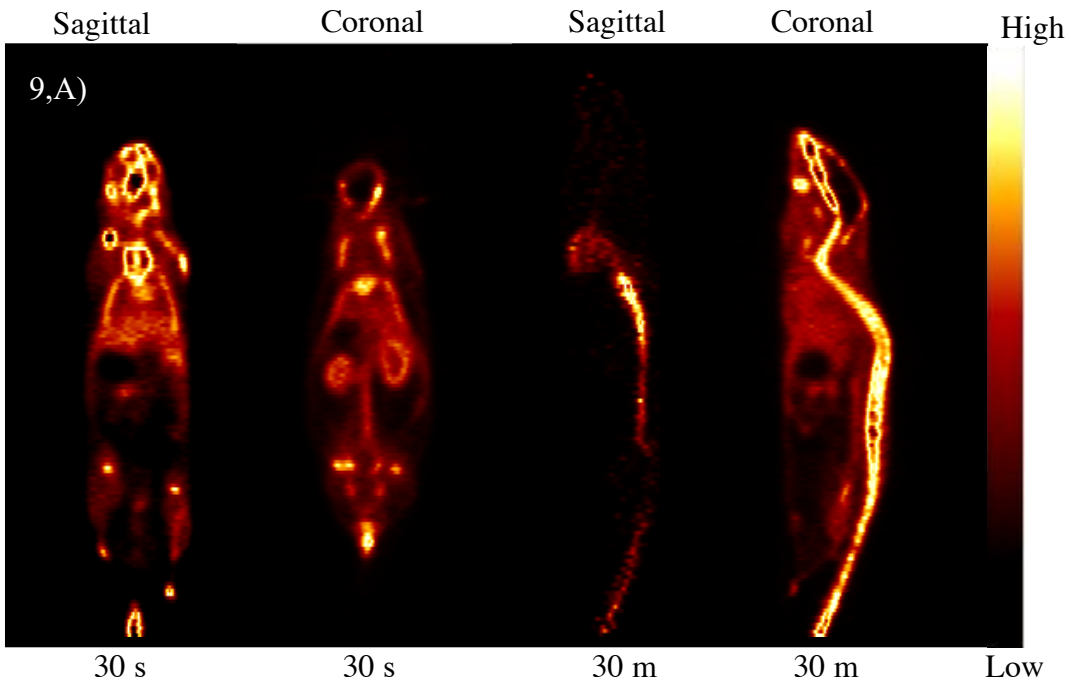

9,B)

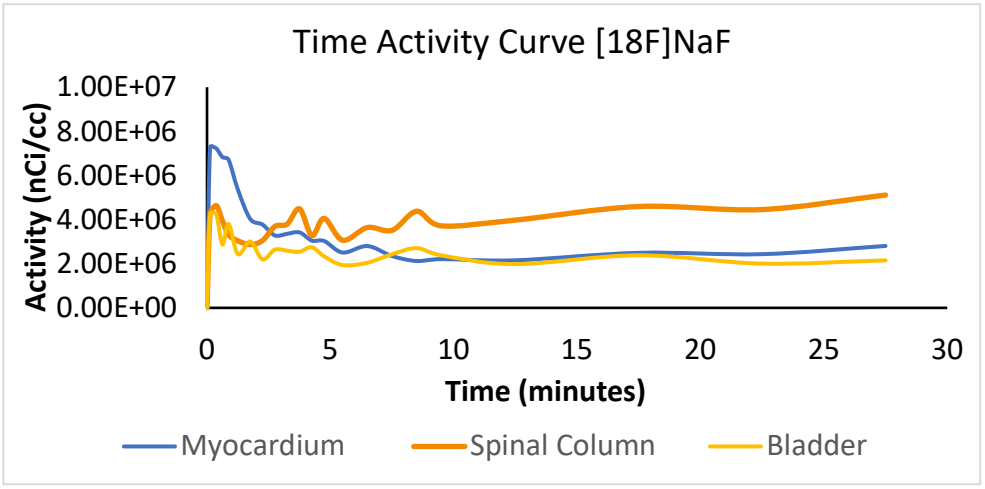

Figure 9: *In vivo* PET and associated time activity curve for [^{18}F]NaF
Animals were injected with approximately 10 µCi/g and activity is measured as percent injected dose/mL over time in minutes. During the 30 minute dynamic PET scan, [^{18}F]NaF is seen passing through the animals vasculature post IV tail-vein injection and then being taken up in bone as it binds to calcium (**A**). Predominantly, activity is seen to be taken up in the spinal column, sternum, and kidneys/bladder as reflected in the time activity curve (**B**).

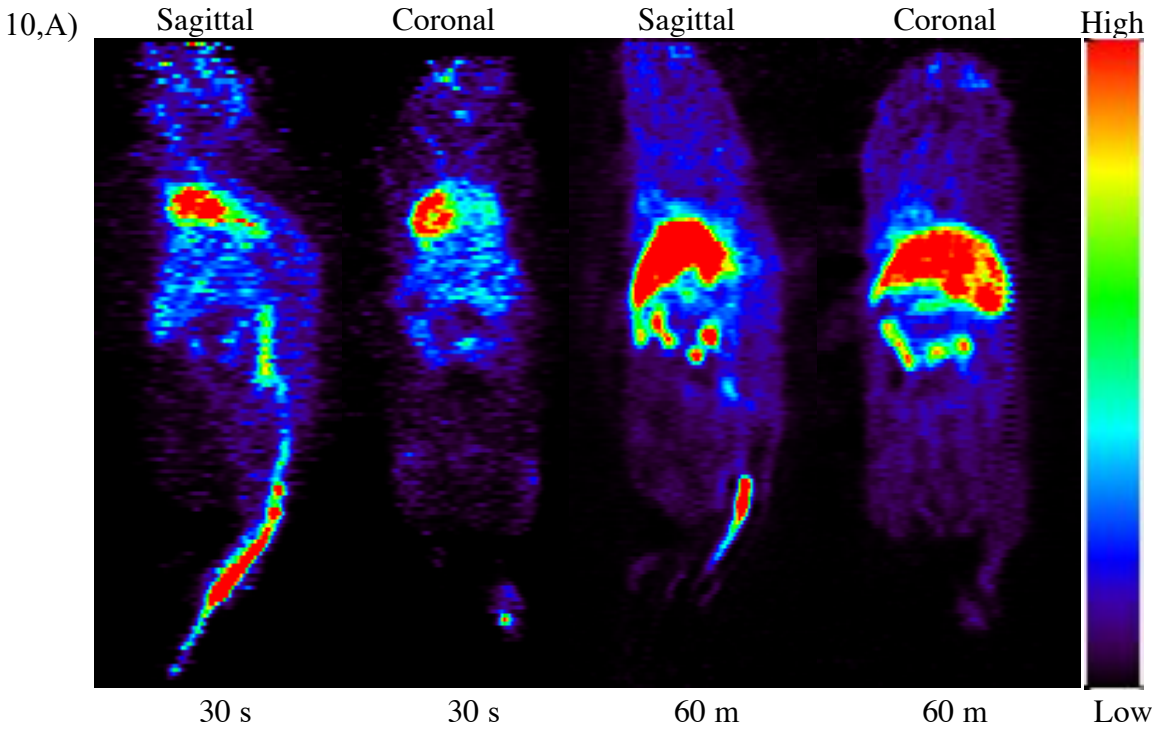

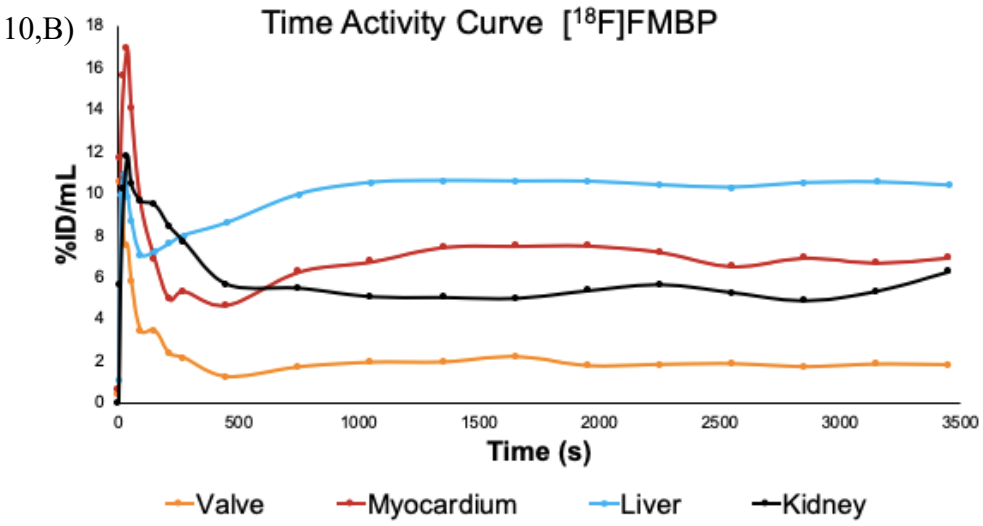

Figure 10: *In vivo* PET and associated time activity curve for [^{18}F]FMBP
Animals were injected with approximately 10 μCi/g and activity is measured as percent injected dose/mL over time in minutes. During the 60 minute dynamic PET scan, [^{18}F]FMBP is seen passing through the animals vasculature post IV tail-vein injection, passing through the myocardium, and then being taken up by the liver for metabolism and excretion through the intestine and kidneys (**A**). Time activity curve shows uptake as a percentage of ID/mL in various organs of interest over time (**B**).

11,A)

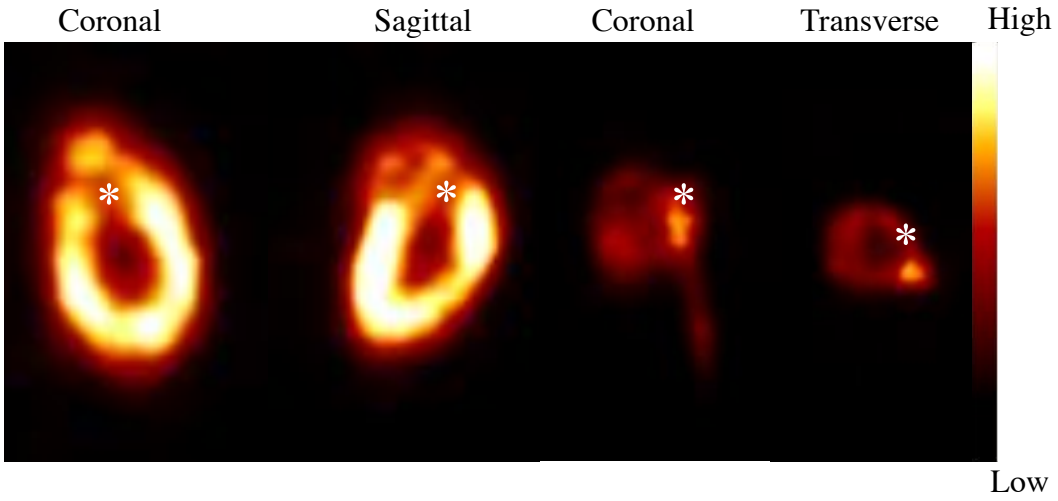

11,B)

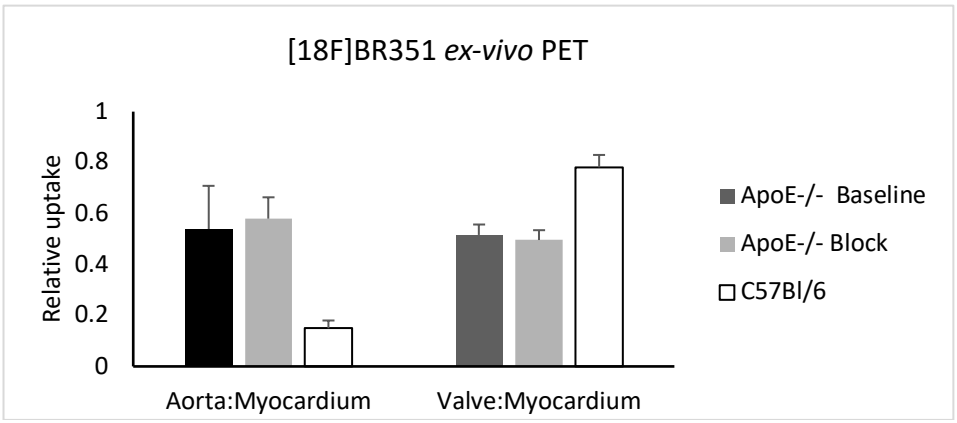

Figure 11: *Ex vivo* PET for [^{18}F]BR351
Animals were injected with approximately 10 μCi/g of radiotracer. After euthanasia, hearts and aortae were harvested and placed in a pitri dish placed within the PET scanner. During the 30 minute static PET scan with [^{18}F]BR351 shows uptake in the myocardium after tissue was harvested 1 hour post IV tracer injection via the tail-vein (**A**). The *ex vivo* PET imaging provides superior resolution to *in vivo* scanning (* denotes the valvular area, ** denotes atherosclerotic plaques within the aorta). *Ex vivo* PET studies with [^{18}F]BR351 were quantified using Amide software where ROIs were drawn around the aorta, valve, and myocardium (**B**) for comparison between baseline and block in ApoE$^{-/-}$ and baseline in WT mice.

3.4 Autoradiography

In vitro autoradiography results suggest specific binding to targets of interest for [^{18}F]FMBP and [^{18}F]BR351 in en face tissue samples (Figure 12A and B). In comparison

between baseline and blocking studies, there was an observed significant decrease between the two for both using [^{18}F]FMBP and [^{18}F]BR351 (P = 0.0062 and P = 0.0394, respectively). Further trials with these radiotracers will be carried out in the near future to build up the sample size and make quantitative measurements for analysis in valve tissue sections.

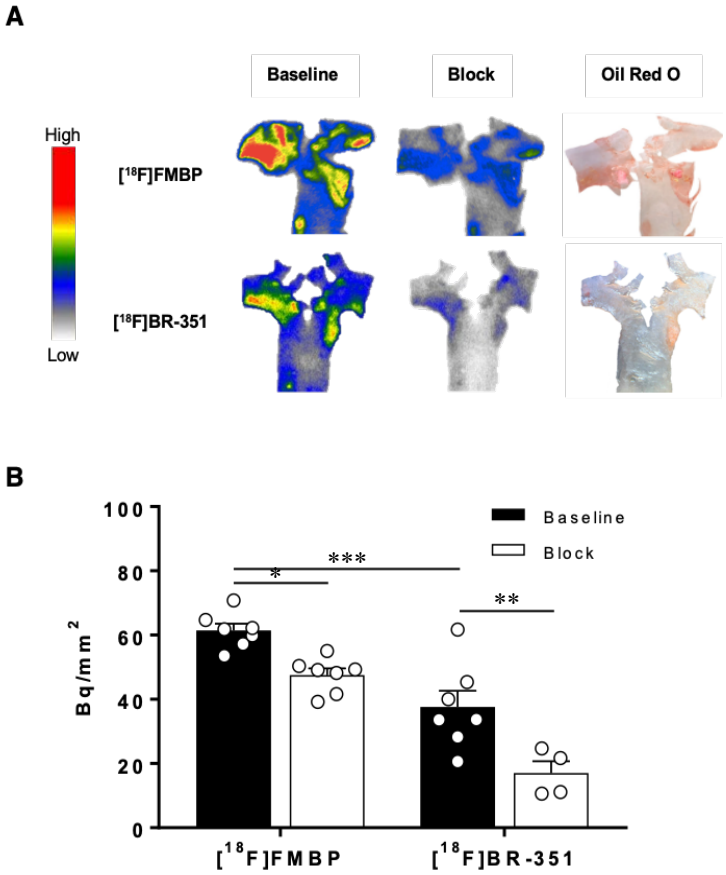

Figure 12: *In vitro* Autoradiography Analysis for [^{18}F]FMBP and [^{18}F]BR351 in en Face Aortae

(**A**) Representative *ApoE*$^{-/-}$ aortic en face *in vitro* autoradiographs 1 hour after incubation with 45 kBq [^{18}F]FMBP or [^{18}F]BR351. Homologous blocking was performed by co-incubation of 2 µM non-radioactive FMBP or BR351. Corresponding bright-field images of ORO stains are shown (n = 4 - 7). (**B**) [^{18}F]FMBP and [^{18}F]BR351 aortic lesion quantification. Two-way ANOVA: ***P = 0.0002, **P = 0.0062, *P = 0.0394. Adapted from Buchler, Munch, and Farber.[55]

Preliminary studies of *in vitro* autoradiography have already been performed using [^{18}F]FMBP (including human tissue evaluation) (Figure 13,A and B, respectively) and [^{18}F]BR351 (Figure 13,C). As this is a preliminary assessment it is hard to draw significant conclusions at this point but with the tissue already harvested and sectioned, autoradiography and related analysis can be completed once tracer production comes back online.

Results suggest that there was no real difference between the baseline group in comparison to the block with this control actually having higher counts within the tissue than baseline. Unlike in the human tissue evaluation, which is in accordance with the above, observed en face aorta tissue (Figure 12), these findings contrast what has been previously shown. As of now, there is no apparent difference between baseline and block in either ApoE$^{-/-}$ or WT tissue samples using BR351 (figure 12,D). Conditions for the pan-MMP tracer still require optimization. With all the tissue for this study now collected and sectioned, the next step will be to compare tracer binding and uptake by autoradiography in 4, 8, and 12 month tissue as well as in healthy and moderate AS, and diseased (calcified) human tissue samples.

Autoradiography was analyzed using ImageJ software. ROIs were calculated by conversion of activity to RLU[*1]which could then be measured as a percentage of light intensity within the ROIs as previously described. Alternatively, autoradiography was analyzed using OptiQuant software. By drawing ROIs around tissue samples, RLU were calculated and then converted to units of activity by using a set of calibrated standard

[*] Relative Light Units: A measurement of luminescence without physical meaning unique to the instrumentation being used and assigned as a proxy for detected radioactive signal by autoradiography. This value is assigned based off of a known signal intensity value.

curves with decay corrected activities (Appendix D – Figures 22 and 23) and measured on the same screen. Activity density (counts/mm^2) was calculated from dividing the sample activity by the area of the ROI. In addition, two ROIs were drawn over the background to subtract out the accounted for noise in the scanned image (Appendix D – Figure 24).

13,A)

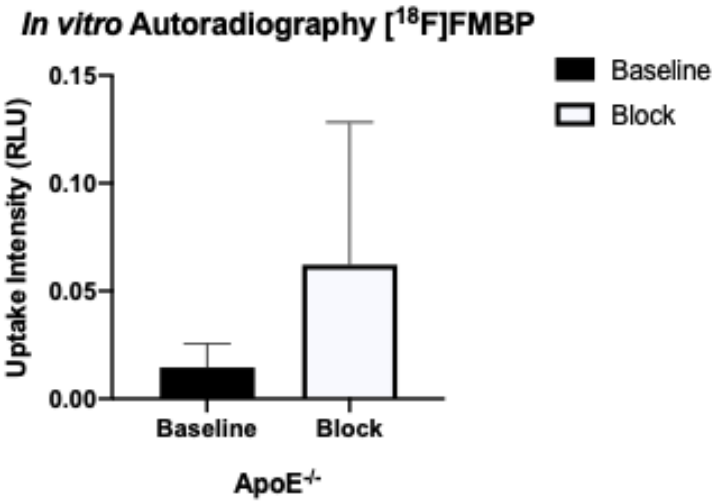

13,B)

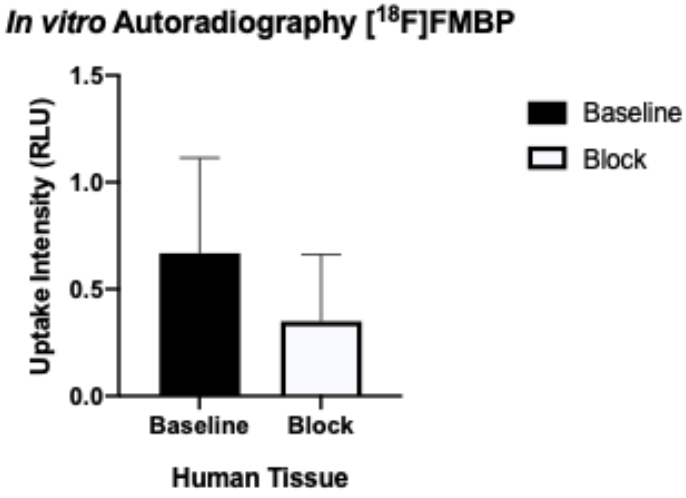

13,C)

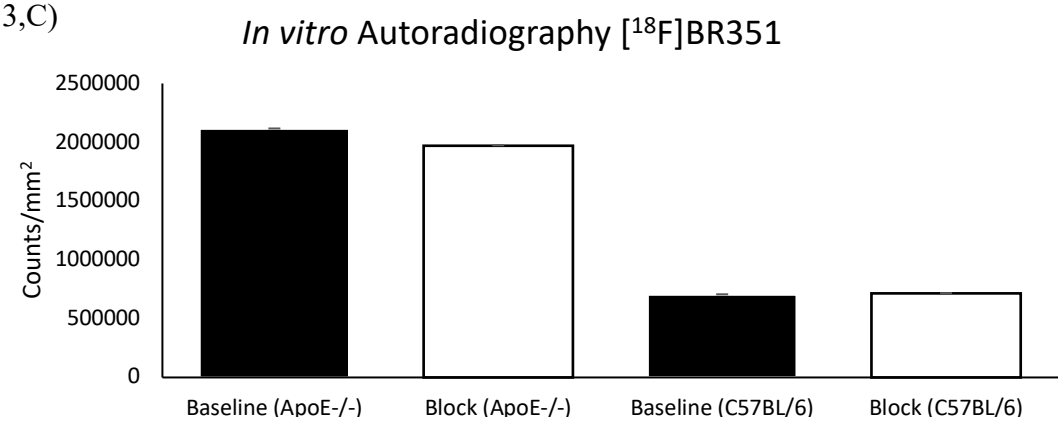

Figure 13: Preliminary Autoradiography Analysis for [^{18}F]FMBP and [^{18}F]BR351
Preliminary assessment of [^{18}F]FMBP in 12-month old ApoE$^{-/-}$ animals (N = 10) (**A**) and human tissue samples of severe aortic stenosis with calcification (N = 4) (**B**). Uptake is measured in relative light units (RLU) and shows comparison between baseline and block. Preliminary assessment of [^{18}F]BR351 *in vitro* autoradiography in 8-month old ApoE$^{-/-}$ and age matched WT animals (N = 6) (**C**). Uptake is measured in counts/mm^2 and shows comparison between baseline and block tissue.

3.5 Human Tissue Histology

Human tissue collected from patients undergoing either heart transplantation or valvular replacement surgery were consented for this study. With their tissue collected, it was then sectioned and stained for confirmation of biomarkers expressed in histological studies as well as tracer uptake via *in vitro* autoradiography. Thus far, expression of calcification, lipid deposition, collagen remodelling, and MMP-13 have been shown to be expressed in the collected tissue.

Following this vein, the same studies (histological sample staining and autoradiography) will be carried out on human tissue samples. All ethics and protocols have been approved tissue collection has commenced.

4.0 Discussion

4.1 Animal model

The predominant experimental animal model selected for this study is the apolipoprotein E-deficient mouse ($ApoE^{-/-}$). The lack of ability to clear lipoproteins from the circulation results in a state of hypercholesteremia that ultimately ends in the formation of atherosclerotic plaques.[45] These atherosclerotic plaques originate around the aortic root and progress throughout the aortic vasculature. Due to a variety of underlying mechanisms (see introduction), these plaques will calcify over time and calcification can also be observed on the leaflets of the aortic valve. This calcification in the lesion and leaflet regions portends the resulting decrease of valve functioning which is believed to impede normal hemodynamics.[15] Therefore, although typically used as a model of atherosclerosis, this knockout model is used extensively for CAVD research and, in this regard, has been

used extensively in research projects of similar design.[3,43] It is believed that several of the causal mechanisms at play tend to overlap in both diseases.[59]

This is not to say that the ApoE$^{-/-}$ mouse is necessarily the most appropriate model for CAVD research. Much attention is also drawn to the low-density-lipoprotein receptor (Ldlr$^{-/-}$) knockout model as well and variations of these models exist with alterations made to genetics and/or diet to induce calcification as this does not occur spontaneously in WT animals.[45,60,61]

Due to several limitations there is an incentive to approach *in vivo* CAVD studies with higher order species such as rabbits and pigs. The main reason being that these animals express a valvular morphology which is more congruent with that of humans. This is with reference to the typical tri-layer extracellular matrix structure (fibrosa, spongiosa, and ventricularis) seen in humans whereas mice only possess valve morphologies which are several cells thick and lack the characteristically separated layers.[62] However, these higher order species possess their own sets of challenges, drawbacks, and limitations as well. For example, rabbits also do not develop spontaneous calcification and housing animals of this size which require additional husbandry can be costly and result in fewer animals in a study.[43] On the other hand, for studies where emphasis is focused on preliminary assessment of expressed biomarkers, the ApoE$^{-/-}$ model is appropriate as these mice, in combination with a western diet, express key biochemical features of disease progression such as; increases in MMP expression (particularly MMP-2 and -9), micro-calcification, and increased macrophage expression.[63] Furthermore, these animals will develop calcification without introduction of a high fat diet but the timeline for them to reach this stage is between 22-30 months.[64] The hemodynamic relevance of this model as

suitable for detecting CAVD still remains a topic of discussion. Given the necessary timelines, genetic and lifestyle habits, compounded with assumptions in clinical modelling needed to be translated to mice; these challenges present considerable limitations.

Of the available animal models though, it is generally agreed that those expressed on a C57Bl/6J background fare superior to others as they are the most likely to develop features of atherosclerosis leading to clinically representative CAVD.[60,61] Lastly, it is worth mentioning other animal models where the approach is focused on a different clinical manifestation of propagated CAVD. This being the atypical BAV phenotype expressed in CAVD patients expressing advanced disease states and which are more likely to be referred for valvular replacement surgery.[6] The underlying issues surrounding these models are in relation to feasibility and degree of disease-like features they develop. In terms of feasibility, these animals tend to not survive given the host of complications that can arise in embryonic development linked to a genetic model with this valvular phenotype.[46,46,65] Furthermore, the incidence rate amongst these animals which actually develop this phenotype is not necessarily certain and in some cases is even below 50%.[9,46,66,65] Some examples of animal models with this phenotypes are the $Nos3^{-/-}$, $Postn^{-/-}$, Gata4, $Gata5^{-/-}$, and $Gata6^{+/-}$.Originally, this study included $Gata6^{+/-}$ mice as they seemed to yield the most promising results but after 12 months the animals had not produced features of CAVD by histology or echocardiography. Compounding these factors, animal model design centred around the approach of a BAV phenotype are not at a stage where they should be used reliably for CAVD research.

4.2 Echocardiography

Echocardiography has long been the gold standard used in the clinical diagnosis and evaluation of CAVD.[67] This imaging modality provides clinicians with a relatively easy method for assessing patients' hemodynamic changes which result from the development of AS preceding disease pathology.[57] In contrast to other detections methods (predominantly CT or catheterization), echocardiography is a relatively inexpensive, quick, and non-invasive tool.[57] Hence the rationale for attempting to emulate the diagnostic power of this imaging modality in mice. Furthermore, it allows for longitudinal studies to be carried out, thereby limiting the total number of animals necessary to complete this study. However, in order for the application to be translatable, the mice used for imaging would have to show hemodynamically relevant AS on top of sharing similarities of key features of disease progression presented as previously mentioned biomarkers of interest.

Unfortunately, this was not observed in the cohort of animals imaged in this study. Interestingly, echocardiographic assessment of disease severity gives limited insight into CAVD pathophysiology and additionally has poor predictive value in determining the rate of progression from early to late stage disease.[67] Although the animals do experience higher velocity and transvalvular pressure gradients (figure 4, A & B), the same is seen in the LVOT of the experimental animals suggesting that this change is not necessarily associated with a change in valve dynamics. This is true, even though by their 8-month timepoint the experimental animals in this study present with a valvular peak velocity well beyond the allotted 1600 mm/s used to classify aortic stenosis in mice.[1,68] This number as baseline for AS classification is based off the averaged baseline value of peak velocity expected in normal healthy mice which is set at half (800 mm/s).[68] The finding of low rates

of hemodynamically significant AS is in accordance with literature reports from this animal model on the specific diet that was used.[63] For reference, this model only develops hemodynamically significant stenosis in less than 2% of cases and only around 9-12 months under these experimental conditions.[43,63]

One of the key features of this animal model is the development of atherosclerotic-like lesions prior to calcification of the related plaques and subsequent calcification of the AV leaflets[43,63,64]. Based on the histological samples obtained from these animals, it is evident that they develop atherosclerotic-like lesions in the LVOT, right below the aortic root. This plaque formation results in a decrease in the LVOT diameter (Figure 4, C) and as a result, aids in predicting a decrease in AVA based on how it is interpreted through the continuity equation (Appendix A – Figure 15). Furthermore, as a result of this decrease, it can be rationalized that the resulting effect is the observed increase in LVOT peak velocity. The same expected mechanism explains observations at the level of the valve since the decrease in AVA yields a higher blood velocity and transvalvular pressure gradient (Figure 1). This is consistent with the observed difference between the experimental and WT animals as the experimental animals develop significantly larger lesions as they age, explaining the decrease in area and increase in velocity and pressure at different timepoints. This decrease in LVOT area, however, is not observed in clinical settings and again calls into question the validity of the animal model in hemodynamic assessment of AS. Typically, in clinic, LVOT diameter should remain constant in patients presenting with AS having the only decrease in diameter being seen in the AVA.[57,69] It is important to note that the measurement at the level of the LVOT was performed in accordance with recordings done in clinical settings where the diameter was measured in the PLAX view

during mid-systole from the white–black interface of the septal endocardium to the anterior mitral leaflet with the acquisition parallel to the aortic valve plane.[57,62] Having touched on the hemodynamics surrounding some of the complications experienced with AS assessment by echocardiography in mice, it also worth noting that there are several assumptions made by clinicians concerning the acquisition and interpretation of computed results.

The mechanism by which the observed increases in pressure and velocity can be explained is by the underlying physical principles at play outlined by the Bernoulli equation (Appendix A – Figure 15). In this case, the Bernoulli principle functions on the premise of the conservation of energy where the potential energy (pressure) and kinetic energy (flow velocity) before the stenotic valve is the same as that after.[70] The transaortic pressure gradient measured by this imaging modality is centered around fundamental equations used in fluid dynamics, specifically, a simplified form of the Bernoulli equation (Appendix A – Figure 15).[57] Thankfully, this process is automated for the sonographer when analyzing the data through the associated software but it is still relevant to understand the physics-based assumptions and to assess the feasibility of their translation between humans and small animals.

The first assumption is that viscous losses and acceleration effects are negligible.[57,70] This is an important point to address as the true assumption being made here is that the flow through the valve is laminar and that the fluid is inviscid. As was observed in several cases, the flow of blood through the AV was turbulent as these animals experienced AR. In these cases, the simplified Bernoulli equation does not hold as this confounding variable of AR added to the presence of potential AS is suggestive of mixed

AV disease.[71] Furthermore, if using the simplified Bernoulli equation in this instance, the velocity at the level of the valve would be grossly overestimated due to the turbulent flow.

The second assumption is that the proximal velocity (LVOT velocity) can be ignored when it is <1 m/s.[57] This is because squaring a number less than one makes it even smaller and it is assumed that the effect it has on the system is negligible when compared to the relatively larger distal velocity.[70] This assumption is key in the simplification of the Bernoulli equation. However, while this may be true in humans, what was observed in this animal model is that the proximal velocity was, in certain instances, above 1 m/s and even sometimes greater than the distal velocity. This was only ever apparent in the early baseline timepoint.

The third and final assumption is that the density of blood in a mouse is the same as the density of blood in humans (1060 kg/m^3) and that it is non-compressible. This assumption is not as important since the relation to human blood is less relevant than is the way the two mediums behave as a fluid in this system. As the equation would suggest, density plays a role in calculating the change in pressure exerted through the valve orifice. However, the variable for density is cancelled out in the simplified equation as the change in height in the system is negligible. The remaining variable for density is simplified further when divided by the standard unit of pressure in pascals converted to mmHg, thus resulting in a value of approximately four (3.975) and a simplified Bernoulli equation represented as:

$$\Delta P = 4v^2$$

The second point with regard to compressibility of blood is important as a fluid which can be compressed would have energy changes within an otherwise linear system and the Bernoulli equation would not hold.

Given the need for such manipulation to simplify a relatively complex system, it stands to reason why these assumptions have been challenged.[70,72] As has been shown already, these assumptions do not necessarily hold true for all the animals used in this study. This ties back to the points made previously concerning the hemodynamic relevance of this model. After careful evaluation in studies surrounding the accuracy of the simplified Bernoulli equation, it has been shown that computational fluid dynamics provides a more accurate depiction of what is truly occurring within the valve.[57,72] The simplified Bernoulli equation still stands as a reasonable assessment of valvular stenosis but should be supplemented with additional measurements from different imaging parameters and should be used with caution in complicated or severe cases of AS.[57,70,72]

Under the circumstances that a unreliable transvalvular pressure gradient, or by extension, AVA, can be calculated from the Bernoulli or continuity equation respectively, there are other metrics that can be assessed to evaluate degree of AS.[57] One of these methods is to assess AVA by planimetry.[57] Placing the probe in the PSAX position and rocking or sliding is rostrally from the level of the papillary muscles within the LV, the orifice area can be measured manually by the user. In addition, it also allows for assessment of valve morphology to determine the presence or absence of the BAV phenotype. However, while this method is feasible in clinic, this is not always the case with mice as there are a multitude of confounding factors which may present additional challenges. For instance, in many cases the sternum casts a shadow over the acoustic

window which decreases visibility of the aortic valve. In addition, in older animals, as they increase in size the same shadowing effect can arise but this time as a result of the lungs occluding the imaging space. Furthermore, in cases where there is severe calcification, the contraction coefficient*[2]may be varied resulting in an underestimation of the AVA.[57] Lastly, it not always possible to have all three leaflets within the same plane given their small size making assessment by planimetry improbable in those cases.

It should also be noted that these animals were imaged under settings resembling normal physiological conditions but in order to have standards which parallel clinical environments, the animals would need to have been trained for imaging under conscious conditions; a task which is overly complicated, time consuming, and not necessarily practical.[57,58] The method by which conscious mice can be scanned imposes additional difficulties on top of what is already a challenging and abstruse modality for small animal imaging.[58]

Individuals attempting similar imaging studies should be familiar with the large learning curve, anatomical knowledge, and intuition necessary with this method of imaging and data acquisition. For example, having the foresight to switch between transducers (in this case between a 550 Hz and a 400 Hz probe) as when peak velocity falls outside the detectable range of the mx550 Hz probe's frequency, the mx400 Hz probe is used to make the necessary measurements. In addition, the 400 Hz probe is more reliable for colour doppler and each probe in this system comes equipped with an optimal focal range that has to be adjusted manually by the sonographer. Furthermore, as is the case in clinical settings,

* Contraction coefficient: A term used in fluid mechanics to describe the proportion between the areas of the stream at the vena contracta (the point in a fluid stream, in this case the valve opening, where the diameter of the stream is the smallest, and fluid velocity is at its maximum) to the area of the orifice.

continuous wave doppler is used to make measurements at the level of the valve for assessing velocity whereas in this system, only pulse-wave doppler is available to the sonographer so there is an increased need from the user to be attentive when recording this measurement in the area of peak velocity (as noted by colour doppler).[57] This is due to the fact that continuous wave doppler requires lower frequency phased-array probes where animal imaging systems are only equipped with high frequency linear probes.

In summary, although standard clinical echocardiography procedures were practiced when studying this animal model, there still exists a whole host of confounding variables which limit the degree of confidence in converting these techniques between humans and murine models. Although at face value it may appear as though the animals develop clinical features of AS preceding CAVD, due to the lack of translatability of clinical echocardiographic assumptions and disease pathophysiology, these findings should act as a guideline and strong consideration when designing future studies of CAVD assessment by echocardiography to ensure best practices.

4.3 Histology

Following hemodynamic assessment via echocardiography, assessment of individual biomarkers of interest, as well as their quantification, was completed using a variety of selective stains and IHC markers. As expected, animals on western diets developed increasing aortic and valvular lesions and as a result underwent extensive matrix remodelling. Lesion size continued to increase proportionately to age in the mice until a certain point where the valve sinus area had reached a level where further increase in lesion size was not possible. Furthermore, there was an evident increase in leaflet remodelling and leaflet size, a key feature of CAVD progression in mice.[1,11,15,59] This is in accordance

with what is typical of this animal model and expected with CAVD.[43] In addition, assessment of calcification and upregulation of inflammatory markers were also observed.

The first biomarker of importance, as the name of the studied pathology would suggest, is calcification. In planning out this study, there came a point where a decision had to be made with regard to methodology of calcification assessment. The choice was between the von Kossa and alizarin red staining procedures. Ultimately, it was decided to use alizarin red for staining of microcalcifications over von Kossa as the latter stains calcium deposits black, which presented with complications in analysis. Given the nature of the animal model used, it is normal to observe black spots within the aortic valve which may be mistaken as a positive calcium stain by von Kossa.[43,73] In reality, these black spots are actually small deposits of neural crest cell melanocytes which arise during arterial valve development in response to the immunological function they play.[73] With regard to the animal model, there was no apparent calcification of the leaflets of $ApoE^{-/-}$ mice until later timepoints. On the other hand, there was visible calcification in the lesion area of the aortic sinus in the older, more stable plaque region of 8-month old mice. The observed calcification is a result of advanced plaques progressing from their inflammatory stage, through lipid deposition and oxidative stress, to calcification.[74,75]

This next feature of disease progression which was evident in the histological samples of diseased animals is from a resulting inflammatory response observed in the form of accumulated macrophages present in newer formed lesion areas (i.e. the hinge region of a lesion). This is also where MMP expression was most notable. MMP-2, -9, and-13 were found to co-localize well with macrophages as was to be expected since macrophages, converted to foam cells, release MMPs to degrade the ECM and allow for

matrix remodelling to occur.[76–78] This is a typical feature of atherosclerosis and advanced plaque progression in CAVD positive mice.[59]

It is important to highlight that in conjuncture to the inflammatory response, active remodelling was observed via the presence of different collagen types in the extracellular matrix of tissue regions of interest. The collagen birefringence was visualized with PSR under polarized light with type I collagen appearing bright yellow/orange and type III collagen being green (figure 2,C). Collagen remodelling takes place once MMPs have degraded the surrounding ECM and new supportive scaffolding can fill its place.[76]

Lastly, *in situ* zymography was completed to determine the presence of activated MMPs. Whereas immunohistochemistry provides insight to MMP expression, zymography specifically identifies those proteases which are active in the tissue region of interest.[79] It is worth mentioning that the results from the zymography study are not shown here as the study had to be put on pause as a result of COVID-19. There were still a significant number of variables which required troubleshooting before the results obtained could be expressed confidently. However, preliminary results have been obtained.

In the animals of later timepoints, active MMPs could be seen by fluorescence in areas of active matrix remodelling in both the leaflet and lesion areas of the sinus. This was expected as these regions underwent active remodelling. For this procedure to work, it was imperative that the tissue be fresh and flash frozen to preserve the enzymatic activity within the tissue. Moreover, all working solutions used had to be maintained at 37 °C to replicate physiological conditions. For the purpose of this study, it was decided to use a pan-MMP substrate as there has been strong data previously presented which draws concerns towards the accuracy of single-MMP based substrate kits, especially with regard

to their use on tissue sections.[3] In the future, collected tissue will be used for gel-based zymography assays as they provide a more clear and reliable method of detection and quantification.[79] Unlike in the tissue-based assay, specific MMP activity can be identified without the need for additional inhibitor studies. In the case of this study, serial sections were obtained at 10 μm (the suggested tissue thickness for zymography studies) and the selected pan-MMP inhibitor used was marimastat with an additional negative control tissue section adjacent being used as well. For reasons that still remain unclear, the block with the pan-MMP inhibitor failed to block the expression signal of the active MMPs. The rationale proposed for this lack of inhibition could be related to the incubating substrate having a higher affinity for the active site and outcompeting the inhibitor used in this study. Moving forward, other inhibitors will be used such as 1,10-phenantroline or ilomastat. Furthermore, with regards to quantification, the results obtained by this zymography procedure are mostly qualitative. Making use of imaging systems such as the In Vivo Imaging System (IVIS) imaging can allow for proper quantitative assessment of zymography results.[3] This is due to the system being able to quantify fluorescent intensity and represent it as a unit per voxel.

4.4 Positron Emission Tomography

Nuclear imaging is a unique method as it is one of the only modalities which images from the inside-out. This allows for administration of target selective radiotracers to identify and monitor unique features of disease and progression. Although, one of the greatest challenges experienced during the PET imaging aspects of this study are largely in part due to the limited spatial resolution available. This holds true even with small animal

imaging systems which have a spatial resolution of about 1.6 +/- 0.06mm.[80] While in theory this should be sufficient for small animal valvular imaging, there are other confounding variables to consider that present additional challenges. For example, respiration rate in the animal, radiotracer spill-over effects, accuracy of transmission scans, and reconstruction algorithms to name a few. Typically, image reconstruction occurs via a transmission scan, in this case done before the dynamic PET study, and makes use of radioactive point sources which are exposed as the animal initially passes through the camera. The transmission scan aids in providing anatomical data to the user for easier localization of tracer binding within the animal. While this is one method of providing such anatomical data, in clinical settings, the trend has now shifted to create hybrid imaging systems which consist of both PET and CT imaging modalities working in unison. The CT scan done in conjuncture with PET allows for superior reconstruction methods and provides sufficiently more accurate anatomical data.[81] Furthermore, the added benefit of CT is that is exposes the individual being scanned to significantly less radiation as lower levels produced by the CT instrument can be filtered out so that they do not reach the patient. This, however, is not really a concern as the exposure is quite low to begin with. This is in contrast with transmission scans which require a long-living isotope point-source to be exposed to the individual being imaged as they pass through the camera. Again, this low level of radiation is not too concerning but it is higher than what would be obtained by CT.

The greater benefit of CT, especially in studies such as this, where one essentially is attempting to image bone, the superior contrast provided by CT would allow for easier co-localization of tracers with areas of valvular calcification. For this to be feasible, however,

the CT would have to be able to provide the appropriate spatial resolution, of which it is indeed capable. This aside, the CT would likely not be able to detect the presence of microcalcifications, hence the need for superior PET imaging agents such as [^{18}F]NaF.

In a clinical setting, AV calcification can be reproducibly measured using [^{18}F]NaF in patients presenting with AS.[51,52] Previously, the most common form of tracer imaging of AS was done by imaging inflammatory responses in the valve using [^{18}F]FDG but these methods were not disease specific.[82] In the case of [^{18}F]NaF, once it is injected through the vasculature, the sodium and fluorine will dissociate and radioactive fluoride is free to interact with hydroxyapatite; a structure composed of a calcium ion surrounded by phosphate groups all used in the coordination of surrounding hydroxy groups.[83] Here the free floating radioactive fluorine ions rapidly exchange with the hydroxy groups forming fluorapatite through a process called chemisorption.[83] The advantage of using [^{18}F]NaF has shown to be far more accurate in measuring disease progression.[82] However, although there is greater specificity using [^{18}F]NaF as opposed to [^{18}F]FDG in AV disease detection, it still faces shortcomings such as spill-over effects from adjacent bones and poor resolution in smaller structures.[84] While imaging via [^{18}F]NaF remains an integral diagnostic tool in imaging valve insufficiencies resulting from advanced calcification, it only provides late stage disease detection and yielding a need for imaging agents at earlier time points in disease progression.[85]

In order of facilitate earlier disease detection there is a need for MMP imaging as its activity is upregulated prior to the formation of calcium deposition and therefore represents a sentinel biomarker of disease pathogenesis.[85] To overcome the aforementioned obstacles related to small animal *in vivo* imagining, an ex vivo imaging approach in small

animals was rationalized. By removing the surrounding tissues and respiratory effects which can increase the likelihood of random events being counted as true events or cardiac motion which obscures small structures in reconstruction, the static ex-vivo PET scan allows for superior resolution and tracer co-localization under more controlled settings. In addition, given the long half-life of $^{18}F^-$, this allows for multiple studies to be performed with the same tissue and thereby limit the total number of animals needed. After the image acquisition has been completed, the tissue can easily be embedded and sectioned for *ex vivo* autoradiography studies.

4.5 Autoradiography

The approach to autoradiography for this study presents itself twofold. Those being by both *ex vivo* and *in vitro* methodologies. The former is meant to provide conditions congruent with those in *in vivo* imaging studies whilst the latter provides insight to target binding and efficiency. It should be noted that due to the COVID-19 pandemic only preliminary assessment of *in vitro* studies have been carried out thus far but promising *in vitro* and *ex vivo* studies have already been observed on en face aortae using the same two radiotracers, the same animal models, and the same dietary conditions for a different study carried out by our group (Figure 11,A and B). At this point it would be inappropriate to draw conclusions on the observed trends in these preliminary studies and should wait until there is a more robust sample size with method optimization carried out in future studies.

In performing autoradiography on histological samples, tissue thickness had to first be optimized to ensure a detectable signal which would be representative of the animal's valve from which it was obtained. In referencing the literature, the most common tissue

thickness used is 20 μm.[86] In contrast to sectioning by frozen samples (10 μm) and paraffin embedded (5 μm) sections, autoradiography has the additional challenge of resolution as radioactivity is read by scanning a phosphor screen which sits on top of the previously tracer-incubated tissue. Originally, we set out to place the full valve sample in the cassette to be exposed to the phosphorous screen but it was quickly determined to be too thick, resulted in poor image quality, and destroyed the tissue samples. Furthermore, it was decided to use fresh, flash frozen tissue to best mimic *in vivo* conditions as opposed to using paraffin embedded tissue which would have to be initially dehydrated and fixed with formalin. Aside from being a long process which would not be agreeable with the half-life of these radiotracers, the drawback to using fixed tissue, although easier to work with and ideal for preserving morphology, is that it crosslinks the proteins and may affect tracer binding in tissue samples by altering target expression patterns.

Choosing to go with the fresh and frozen tissue samples embedded in OCT, thickness was then increased from 10 μm to 30 μm with serial sections obtained on the same slide to ensure they were exposed to the same treatment. Tissue sections at 30 μm were challenging to place on slides and in addition, were more likely to come off when pre-washing tissue to remove the surrounding OCT in preparation for tracer incubation. Furthermore, tissue at 10 μm showed limited expression as a result of the limited target density available for scanning. It was decided to continue with 20 μm tissue sections as suggested in literature of similar study design as this produced the best and most consistent results. Serial sections could be easily obtained from tissue samples and then incubated under same conditions. Similar methods were carried out for the human tissue samples.

5.0 Conclusion

As is made evident in the data and analysis conducted for this study, there still remains several concerns regarding the appropriateness of the animal models typically used in CAVD research. Until one can be provided that is CAVD specific, the exact molecular mechanism by which the disease manifests in murine models cannot be confidently used as a proxy for studying disease development in humans. As was shown by echocardiography, the preceding AS seen in clinical evaluations leading to CAVD are not observed to the same degree in the animal model used. That being said, the presence of overlapping biomarkers seen in both human and murine models provide insight to key targets of interest from a nuclear and molecular imaging standpoint. With advancements being made in imaging modalities, tracer production and formulation, as well as genetic models for studying CAVD, it is reasonable to conclude that steps can be taken forward in the near future to make important differences in the way CAVD is managed and treated in a clinical setting.

In the future, several other studies will be carried out to better assess the animal models used for studying CAVD. In addition, further comparison will be made in reference to the biomarkers expressed in human tissue with samples currently being collected and processed for these studies. In addition, we plan to move our pan-MMP zymography imaging from a qualitative space towards a more definitive single MMP assessment and a quantitative approach using IVIS imaging systems which will soon become available. Several preliminary assessments have already indicated promising results for both human and imaging studies, respectively. Furthermore, new iterations of previous and diverse radiotracers are being produced to image alternative targets of interest upregulated in early

stages of disease pathophysiology. Lastly, an attempt will be made to evaluate existing tracers used for this study in higher order species that are more reflective of clinical presentations of CAVD.

The findings obtained in this study will serve to model next generation projects focused on assessment of CAVD progression in murine models. Given the results obtained by echocardiography, the nature of the animal model used and how it relates to hemodynamic assessment have been well elucidated and highlight several key limitations one should consider when designing similar studies. That being said, assessment of valve morphology has shown to be quite feasible given sufficient practice and ensuring that hemodynamically significant parameters are maintained.

In terms of characterizing biomarkers of interest, the findings presented here suggest upregulation of various biomarkers of interest such as MMP-2, -9, and -13 in diseased animals in comparison to their WT controls. This serves as evidence of disease progression within the animal model used and it has been shown that these same targets are well suited candidates for future nuclear molecular imaging projects given their high degree of specificity.

This translational project will aid in providing a better understanding of valvular heart disease pathophysiology, identifying potential therapeutic targets, and developing and testing these agents. In addition, the use of less and non-invasive imaging modalities to predict or diagnose the onset of CAVD provides an alternative to current standards of care which have the potential to introduce other secondary complications on top of pre-existing associated risk factors. A molecular imaging agent capable of predicting CAVD will lay

the groundwork for necessary therapies, obviate the need for redundant animal models, and diminish disease related disparities.

References

1. Scatena M, Jackson MF, Speer MY, Leaf EM, Wallingford MC, Giachelli CM. Increased Calcific Aortic Valve Disease in response to a diabetogenic, procalcific diet in the LDLr−/−ApoB100/100 mouse model. *Cardiovasc Pathol*. 2018;34:28-37. doi:10.1016/j.carpath.2018.02.002

2. Lindman BR, Clavel M-A, Mathieu P, et al. Calcific aortic stenosis. *Nat Rev Dis Primers*. 2016;2(1):16006. doi:10.1038/nrdp.2016.6

3. Jung J-J, Razavian M, Kim H-Y, et al. Matrix metalloproteinase inhibitor, doxycycline and progression of calcific aortic valve disease in hyperlipidemic mice. *Sci Rep*. 2016;6(1):32659. doi:10.1038/srep32659

4. Nguyen V, Michel M, Eltchaninoff H, et al. Implementation of Transcatheter Aortic Valve Replacement in France. *Journal of the American College of Cardiology*. 2018;71(15):1614-1627. doi:10.1016/j.jacc.2018.01.079

5. Lerman DA, Prasad S, Alotti N. Calcific Aortic Valve Disease: Molecular Mechanisms and Therapeutic Approaches. *Eur Cardiol*. 2015;10(2):108-112. doi:10.15420/ecr.2015.10.2.108

6. Roberts WC, Ko JM. Frequency by Decades of Unicuspid, Bicuspid, and Tricuspid Aortic Valves in Adults Having Isolated Aortic Valve Replacement for Aortic Stenosis, With or Without Associated Aortic Regurgitation. *Circulation*. 2005;111(7):920-925. doi:10.1161/01.CIR.0000155623.48408.C5

7. Otto CM, Prendergast B. Aortic-Valve Stenosis — From Patients at Risk to Severe Valve Obstruction. *New England Journal of Medicine*. 2014;371(8):744-756. doi:10.1056/NEJMra1313875

8. Sathyamurthy I, Alex S, Kirubakaran K, Sengottuvelu G, Srinivasan KN. Risk factor profile of calcific aortic stenosis. *Indian Heart J*. 2016;68(6):828-831. doi:10.1016/j.ihj.2016.04.007

9. Gharibeh L, Komati H, Bossé Y, et al. GATA6 Regulates Aortic Valve Remodeling, and Its Haploinsufficiency Leads to Right-Left Type Bicuspid Aortic Valve. *Circulation*. 2018;138(10):1025-1038. doi:10.1161/CIRCULATIONAHA.117.029506

10. Martin PS, Kloesel B, Norris RA, Lindsay M, Milan D, Body SC. Embryonic Development of the Bicuspid Aortic Valve. *J Cardiovasc Dev Dis*. 2015;2(4):248-272. doi:10.3390/jcdd2040248

11. Sathyamurthy I, Alex S. Calcific aortic valve disease: Is it another face of atherosclerosis? *Indian Heart J*. 2015;67(5):503-506. doi:10.1016/j.ihj.2015.07.033

12. Li C, Xu S, Gotlieb AI. The progression of calcific aortic valve disease through injury, cell dysfunction, and disruptive biologic and physical force feedback loops. *Cardiovasc Pathol*. 2013;22(1):1-8. doi:10.1016/j.carpath.2012.06.005

13. Liu AC, Joag VR, Gotlieb AI. The Emerging Role of Valve Interstitial Cell Phenotypes in Regulating Heart Valve Pathobiology. *Am J Pathol*. 2007;171(5):1407-1418. doi:10.2353/ajpath.2007.070251

14. Mathieu P, Boulanger M-C. Basic Mechanisms of Calcific Aortic Valve Disease. *Canadian Journal of Cardiology*. 2014;30(9):982-993. doi:10.1016/j.cjca.2014.03.029

15. Miller JD, Weiss RM, Heistad DD. Calcific Aortic Valve Stenosis: Methods, Models, and Mechanisms. *Circ Res*. 2011;108(11):1392-1412. doi:10.1161/CIRCRESAHA.110.234138

16. Skowasch D, Schrempf S, Wernert N, et al. Cells of primarily extra-valvular origin in degenerative aortic valves and bioprostheses. *Eur Heart J*. 2005;26(23):2576-2580. doi:10.1093/eurheartj/ehi458

16. Yoder MC, Mead LE, Prater D, Krier TR, Mroueh KN, Li F, Kraisch R, Temm CJ, Prchal JT, Ingram DA. Redefining endothelial progenitor cells via clonal analysis and hematopoietic stem/progenitor cell principals. *Blood*. 2007;109(5):1801-1809.

17. Visconti RP, Ebihara Y, LaRue AC, Fleming P, McQuinn TC, Masuya M, Minamiguchi H, Markwald RR, Ogawa M, Drake CJ. An in vivo analysis of hematopoietic stem cell potential: hematopoietic origin of cardiac valve interstitial cells. Circ Res. 2006;98(5):690-696. doi:10.1161/01.RES.0000207384.81818.d4

19. Durbin AD, Gotlieb AI. Advances towards understanding heart valve response to injury. *Cardiovasc Pathol*. 2002;11(2):69-77. doi:10.1016/s1054-8807(01)00109-0

19. Desmoulière A, Badid C, Bochaton-Piallat ML, Gabbiani G. Apoptosis during wound healing, fibrocontractive diseases and vascular wall injury. Int J Biochem Cell Biol. 1997;29(1):19-30. doi:10.1016/s1357-2725(96)00117-3

21. Jian B, Narula N, Li Q, Mohler ER, Levy RJ. Progression of aortic valve stenosis: TGF-beta1 is present in calcified aortic valve cusps and promotes aortic valve interstitial cell calcification via apoptosis. *Ann Thorac Surg*. 2003;75(2):457-465; discussion 465-466. doi:10.1016/s0003-4975(02)04312-6

22. Chen J-H, Yip CYY, Sone ED, Simmons CA. Identification and characterization of aortic valve mesenchymal progenitor cells with robust osteogenic calcification potential. *Am J Pathol*. 2009;174(3):1109-1119. doi:10.2353/ajpath.2009.080750

23. Masjedi S, Lei Y, Patel J, Ferdous Z. Sex-related differences in matrix remodeling and early osteogenic markers in aortic valvular interstitial cells. *Heart Vessels*. 2017;32(2):217-228. doi:10.1007/s00380-016-0909-8

23. Bäck M, Hansson G. Mechanism of Atherosclerosis - an overview. In: de Lemos J, Omland T. Chronic Coronary Artery Disease. Elseive, 2018,45-54

25. Cai J, Pardali E, Sánchez-Duffhues G, ten Dijke P. BMP signaling in vascular diseases. *FEBS Lett*. 2012;586(14):1993-2002. doi:10.1016/j.febslet.2012.04.030

26. Sucosky P, Balachandran K, Elhammali A, Jo H, Yoganathan AP. Altered Shear Stress Stimulates Upregulation of Endothelial VCAM-1 and ICAM-1 in a BMP-4–and TGF-β1–Dependent Pathway. *Arterioscler Thromb Vasc Biol*. 2009;29(2):254-260. doi:10.1161/ATVBAHA.108.176347

27. Csiszar A, Labinskyy N, Jo H, Ballabh P, Ungvari Z. Differential proinflammatory and prooxidant effects of bone morphogenetic protein-4 in coronary and pulmonary arterial endothelial cells. *Am J Physiol Heart Circ Physiol*. 2008;295(2):H569-577. doi:10.1152/ajpheart.00180.2008

28. Miller JD, Weiss RM, Serrano KM, et al. Evidence for active regulation of pro-osteogenic signaling in advanced aortic valve disease. *Arterioscler Thromb Vasc Biol*. 2010;30(12):2482-2486. doi:10.1161/ATVBAHA.110.211029

29. Miller JD, Weiss RM, Serrano KM, et al. Lowering plasma cholesterol levels halts progression of aortic valve disease in mice. *Circulation*. 2009;119(20):2693-2701. doi:10.1161/CIRCULATIONAHA.108.834614

30. Osman L, Yacoub MH, Latif N, Amrani M, Chester AH. Role of human valve interstitial cells in valve calcification and their response to atorvastatin. *Circulation*. 2006;114(1 Suppl):I547-552. doi:10.1161/CIRCULATIONAHA.105.001115

31. Mathieu P, Voisine P, Pépin A, Shetty R, Savard N, Dagenais F. Calcification of human valve interstitial cells is dependent on alkaline phosphatase activity. *J Heart Valve Dis*. 2005;14(3):353-357.

32. Warnock JN, Burgess SC, Shack A, Yoganathan AP. Differential immediate-early gene responses to elevated pressure in porcine aortic valve interstitial cells. *J Heart Valve Dis*. 2006;15(1):34-41; discussion 42.

33. Rajamannan NM, Subramaniam M, Caira F, Stock SR, Spelsberg TC. Atorvastatin Inhibits Hypercholesterolemia-Induced Calcification in the Aortic Valves via the Lrp5 Receptor Pathway. *Circulation*. 2005;112(9 0):I229-I234. doi:10.1161/01.CIRCULATIONAHA.104.524306

34. Gu G, Chen T, Zhou H, Sun K, Li J. Role of Wnt/β-catenin signaling pathway in the mechanism of calcification of aortic valve. *J Huazhong Univ Sci Technol [Med Sci]*. 2014;34(1):33-36. doi:10.1007/s11596-014-1228-x

35. Little RD, Carulli JP, Del Mastro RG, et al. A Mutation in the LDL Receptor–Related Protein 5 Gene Results in the Autosomal Dominant High–Bone-Mass Trait. *Am J Hum Genet*. 2002;70(1):11-19.

35. Gong Y, Slee RB, Fukai N, ...Warman ML. LDL Receptor-Related Protein 5 (LRP5) Affects Bone Accrual and Eye Development.*Cell*. 2001;107(4):513-523. Doi: 10.1016/S0092-8674(01)00571-2

37. Caira FC, Stock SR, Gleason TG, et al. Human Degenerative Valve Disease Is Associated With Up-Regulation of Low-Density Lipoprotein Receptor-Related Protein 5 Receptor-Mediated Bone Formation. *J Am Coll Cardiol*. 2006;47(8):1707-1712. doi:10.1016/j.jacc.2006.02.040

38. Nagase H, Visse R, Murphy G. Structure and function of matrix metalloproteinases and TIMPs. *Cardiovascular Research*. 2006;69(3):562-573. doi:10.1016/j.cardiores.2005.12.002

39. Fondard O, Detaint D, Iung B, et al. Extracellular matrix remodelling in human aortic valve disease: the role of matrix metalloproteinases and their tissue inhibitors. *European Heart Journal*. 2005;26(13):1333-1341. doi:10.1093/eurheartj/ehi248

40. Kossar AP, Anselmo W, Grau JB, et al. Circulating and tissue matricellular RNA and protein expression in calcific aortic valve disease. *Physiological Genomics*. 2020;52(4):191-199. doi:10.1152/physiolgenomics.00104.2019

41. Kaden JJ, Dempfle C-E, Grobholz R, et al. Inflammatory regulation of extracellular matrix remodeling in calcific aortic valve stenosis. *Cardiovascular Pathology*. 2005;14(2):80-87. doi:10.1016/j.carpath.2005.01.002

42. Foley CJ, Kuliopulos A. Mouse Matrix Metalloprotease-1a (Mmp1a) Gives New Insight Into MMP Function. *J Cell Physiol*. 2014;229(12):1875-1880. doi:10.1002/jcp.24650

43. Sider KL, Blaser MC, Simmons CA. Animal Models of Calcific Aortic Valve Disease. *International Journal of Inflammation*. 2011;2011:1-18. doi:10.4061/2011/364310

44. Reference GH. APOE gene. Genetics Home Reference. Accessed January 20, 2020. https://ghr.nlm.nih.gov/gene/APOE

45. Lo Sasso G, Schlage WK, Boué S, Veljkovic E, Peitsch MC, Hoeng J. The Apoe−/− mouse model: a suitable model to study cardiovascular and respiratory diseases in the context of cigarette smoke exposure and harm reduction. *J Transl Med*. 2016;14. doi:10.1186/s12967-016-0901-1

46. Laforest B, Andelfinger G, Nemer M. Loss of Gata5 in mice leads to bicuspid aortic valve. *J Clin Invest*. 2011;121(7):2876-2887. doi:10.1172/JCI44555

47. Rinnström D, Engström KG, Johansson B. Subtypes of bicuspid aortic valves in coarctation of the aorta. *Heart Vessels*. 2014;29(3):354-363. doi:10.1007/s00380-013-0370-x

43. Cherry S, Sorenson J, Phelps M. *Physics in Nuclear Medicine.* 4th ed. Saunders; 2012.

49. Cocker MS. [18F]-NaF PET/CT Identifies Active Calcification in Carotid Plaque. :3.

50. McKenney-Drake ML, Moghbel MC, Paydary K, et al. 18F-NaF and 18F-FDG as molecular probes in the evaluation of atherosclerosis. *Eur J Nucl Med Mol Imaging*. 2018;45(12):2190-2200. doi:10.1007/s00259-018-4078-0

51. Dweck MR, Jenkins WSA, Vesey AT, et al. 18F-sodium fluoride uptake is a marker of active calcification and disease progression in patients with aortic stenosis. *Circ Cardiovasc Imaging*. 2014;7(2):371-378. doi:10.1161/CIRCIMAGING.113.001508

52. Hyafil F, Messika-Zeitoun D, Burg S, et al. Detection of ^{18}fluoride sodium accumulation by positron emission tomography in calcified stenotic aortic valves. *Am J Cardiol*. 2012;109(8):1194-1196. doi:10.1016/j.amjcard.2011.11.060

53. Perrotta I, Russo E, Camastra C, et al. New evidence for a critical role of elastin in calcification of native heart valves: immunohistochemical and ultrastructural study with literature review. *Histopathology*. 2011;59(3):504-513. doi:10.1111/j.1365-2559.2011.03977.x

54. Wagner S, Breyholz H-J, Law MP, et al. Novel Fluorinated Derivatives of the Broad-Spectrum MMP Inhibitors N-Hydroxy-2(R)-[[(4-methoxyphenyl)sulfonyl](benzyl)- and (3-picolyl)-amino]-3-methyl-butanamide as Potential Tools for the Molecular Imaging of Activated MMPs with PET. *J Med Chem*. 2007;50(23):5752-5764. doi:10.1021/jm0708533

55. Buchler A, Munch M, Farber G, Zhao X, Al Haddad R, Rotstein BH. Selective Imaging of Matrix Metalloproteinase-13 to Detect Extracellular Matrix Remodeling in Atherosclerotic Lesions. *In Preperation*. Published online May 2020.

56. Vazquez N, Missault S, Vangestel C, et al. Evaluation of [18F]BR420 and [18F]BR351 as radiotracers for MMP-9 imaging in colorectal cancer. *Journal of Labelled Compounds and Radiopharmaceuticals*. 2017;60(1):69-79. doi:10.1002/jlcr.3476

57. Baumgartner H, Hung J, Bermejo J, et al. Echocardiographic assessment of valve stenosis: EAE/ASE recommendations for clinical practice. *Eur J Echocardiogr*. 2009;10(1):1-25. doi:10.1093/ejechocard/jen303

58. Gao S, Ho D, Vatner DE, Vatner SF. Echocardiography in Mice. *Curr Protoc Mouse Biol*. 2011;1:71-83. doi:10.1002/9780470942390.mo100130

59. Fazio S, Linton MF. Mouse models of hyperlipidemia and atherosclerosis. *Front Biosci*. 2001;6:D515-525. doi:10.2741/fazio

60. Daugherty A, Rateri DL. Development of experimental designs for atherosclerosis studies in mice. *Methods*. 2005;36(2):129-138. doi:10.1016/j.ymeth.2004.11.008

55. Dansky HM, Charlton SA, Sikes JL, Heath SC, Simantov R, Levin LF, Shu P, Moore KJ, Breslow JL, Smith JD. Genetic Background Determines the Extent of Atherosclerosis in ApoE-Deficient Mice. *Arterioscler Thromb Vasc* Biol. 1999;19:1960-1968. Doi: https://doi.org/10.1161/01.ATV.19.8.1960

62. Hinton RB, Alfieri CM, Witt SA, et al. Mouse heart valve structure and function: echocardiographic and morphometric analyses from the fetus through the aged adult. *Am J Physiol Heart Circ Physiol*. 2008;294(6):H2480-2488. doi:10.1152/ajpheart.91431.2007

63. Aikawa Elena, Nahrendorf Matthias, Sosnovik David, et al. Multimodality Molecular Imaging Identifies Proteolytic and Osteogenic Activities in Early Aortic Valve Disease. *Circulation*. 2007;115(3):377-386. doi:10.1161/CIRCULATIONAHA.106.654913

64. Tanaka K, Sata M, Fukuda D, et al. Age-associated aortic stenosis in apolipoprotein E-deficient mice. *J Am Coll Cardiol*. 2005;46(1):134-141. doi:10.1016/j.jacc.2005.03.058

65. Yang B, Zhou W, Jiao J, et al. Protein-altering and regulatory genetic variants near GATA4 implicated in bicuspid aortic valve. *Nature Communications*. 2017;8(1):1-10. doi:10.1038/ncomms15481

60. Lee TC, Zhao YD, Courtman DW, Stewart DJ. Abnormal Aortic Valve Development in Mice Lacking Endothelial Nitric Oxide Synthase. *Circulation*. 2000;101:2345-2348.10.1161/01.CIR.101.20.2345

67. Small A, Kiss D, Giri J, et al. Biomarkers of Calcific Aortic Valve Disease. *Arterioscler Thromb Vasc Biol*. 2017;37(4):623-632. doi:10.1161/ATVBAHA.116.308615

68. Drolet M-C, Roussel E, Deshaies Y, Couet J, Arsenault M. A High Fat/High Carbohydrate Diet Induces Aortic Valve Disease in C57BL/6J Mice. *Journal of the American College of Cardiology*. 2006;47(4):850-855. doi:10.1016/j.jacc.2005.09.049

69. Rajamannan NM, Evans FJ, Aikawa E, et al. Calcific Aortic Valve Disease: Not Simply a Degenerative Process A Review and Agenda for Research from the National Heart and Lung and Blood Institute Aortic Stenosis Working Group. *Circulation*. 2011;124(16):1783-1791. doi:10.1161/CIRCULATIONAHA.110.006767

70. Scantlebury DC, Geske JB, Nishimura RA. Limitations of Doppler Echocardiography in the Evaluation of Serial Stenoses. *Circ Cardiovasc Imaging*. 2013;6(5):850-852. doi:10.1161/CIRCIMAGING.113.000575

71. Stumm MV, Petersen J, Westermann D, Reichenspurner H, Girdauskas E. Treatment strategies for mixed aortic valve disease in nonelderly patients. *Expert Review of Cardiovascular Therapy*. 2019;17(12):873-882. doi:10.1080/14779072.2019.1702520

72. Heys JJ, Holyoak N, Calleja AM, Belohlavek M, Chaliki HP. Revisiting the Simplified Bernoulli Equation. *Open Biomed Eng J*. 2010;4:123-128. doi:10.2174/1874120701004010123

73. Sánchez-Piña J, Lorenzale M, Fernández MC, Durán AC, Sans-Coma V, Fernández B. Pigmentation of the aortic and pulmonary valves in C57BL/6J x Balb/cByJ hybrid mice of different coat colours. *Anat Histol Embryol*. 2019;48(5):429-436. doi:10.1111/ahe.12463

68. Pomerance A. Pathogenesis of aortic stenosis and its relation to age. *BR Heart J*. 1972;34(6):569-574. Doi: 10.1136/hrt.34.6.569

75. Kim EJ, Song BG, Sohn HR, et al. Senile Cardiac Calcification Syndrome: A Rare Case of Extensive Calcification of Left Ventricular Papillary Muscle. *Cardiol Res*. 2011;2(3):127-129. doi:10.4021/cr29w

76. Fondard O, Detaint D, Iung B, et al. Extracellular matrix remodelling in human aortic valve disease: the role of matrix metalloproteinases and their tissue inhibitors. *European Heart Journal*. 2005;26(13):1333-1341. doi:10.1093/eurheartj/ehi248

77. Newby AC, George SJ, Ismail Y, Johnson JL, Sala-Newby GB, Thomas AC. Vulnerable atherosclerotic plaque metalloproteinases and foam cell phenotypes. *Thromb Haemost*. 2009;101(6):1006-1011.

78. Elkington PT, Green JA, Friedland JS. Analysis of Matrix Metalloproteinase Secretion by Macrophages. In: Reiner NE, ed. *Macrophages and Dendritic Cells: Methods and Protocols*. Methods in Molecular Biology™. Humana Press; 2009:253-265. doi:10.1007/978-1-59745-396-7_16

73. Yan, SJ, Blomme EAG. In Situ Zymography: A Molecular Pathology Technique to Localize Endogenous Protease Activity in Tissue Sections. Veterinary Pathology. 2003;40(3):227–236. https://doi.org/10.1354/vp.40-3-227

80. Visser EP, Disselhorst JA, Brom M, et al. Spatial Resolution and Sensitivity of the Inveon Small-Animal PET Scanner. *J Nucl Med*. 2009;50(1):139-147. doi:10.2967/jnumed.108.055152

81. Ederhy S, Mansencal N, Réant P, Piriou N, Barone-Rochette G. Role of multimodality imaging in the diagnosis and management of cardiomyopathies. *Archives of Cardiovascular Diseases*. 2019;112(10):615-629. doi:10.1016/j.acvd.2019.07.004

82. Jenkins WSA, Vesey AT, Shah ASV, et al. Valvular ^{18}F-Fluoride and ^{18}F-Fluorodeoxyglucose Uptake Predict Disease Progression and Clinical Outcome in Patients With Aortic Stenosis. *Journal of the American College of Cardiology*. 2015;66(10):1200-1201. doi:10.1016/j.jacc.2015.06.1325

83. Czernin J, Satyamurthy N, Schiepers C. Molecular Mechanisms of Bone 18F-NaF Deposition. *J Nucl Med*. 2010;51(12):1826-1829. doi:10.2967/jnumed.110.077933

84. Blomberg BA, Thomassen A, Jong PA de, et al. Impact of Personal Characteristics and Technical Factors on Quantification of Sodium 18F-Fluoride Uptake in Human Arteries: Prospective Evaluation of Healthy Subjects. *J Nucl Med*. 2015;56(10):1534-1540. doi:10.2967/jnumed.115.159798

85. Farber G, Boczar KE, Wiefels CC, et al. The Future of Cardiac Molecular Imaging. *Seminars in Nuclear Medicine*. Published online March 17, 2020. doi:10.1053/j.semnuclmed.2020.02.005

86. Linares A, Couling LE, Carrera EJ, Speth RC. Receptor Autoradiography Protocol for the Localized Visualization of Angiotensin II Receptors. *J Vis Exp*. 2016;(112). doi:10.3791/53866

Appendix

Appendix A – Background and Supporting Information

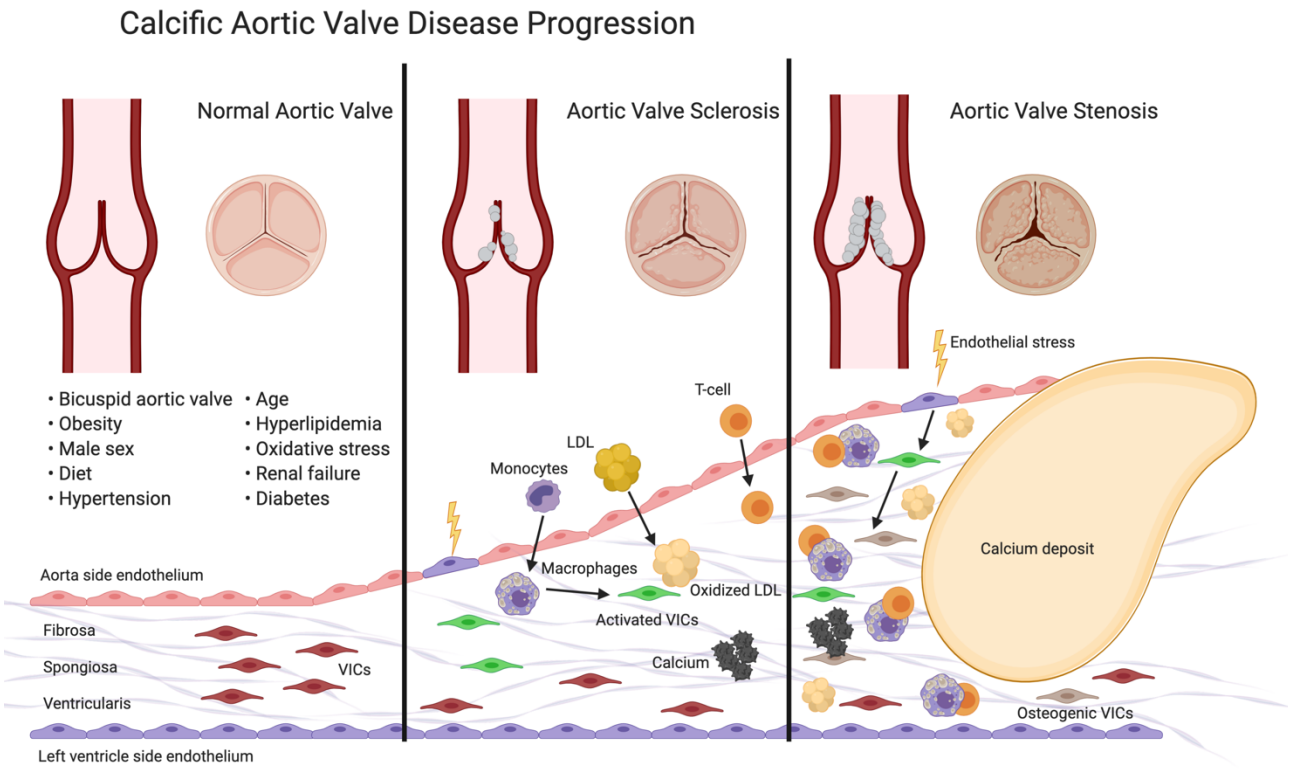

Figure 14: Calcific Aortic Valve Disease
Progression of calcific aortic valve disease from a normal healthy valve, through aortic sclerosis, and ending in aortic stenosis with presence of calcium nodules. Several risk factors believed to be involved in disease pathogenesis as well potential molecular markers are outlined as well. Furthermore, conversion of quiescent VICs to osteogenic VICs is outlined as well. Adapted from Farber, Boczar, Wiefels, et al.[85] Made with Biorender©

Bernoulli Equation

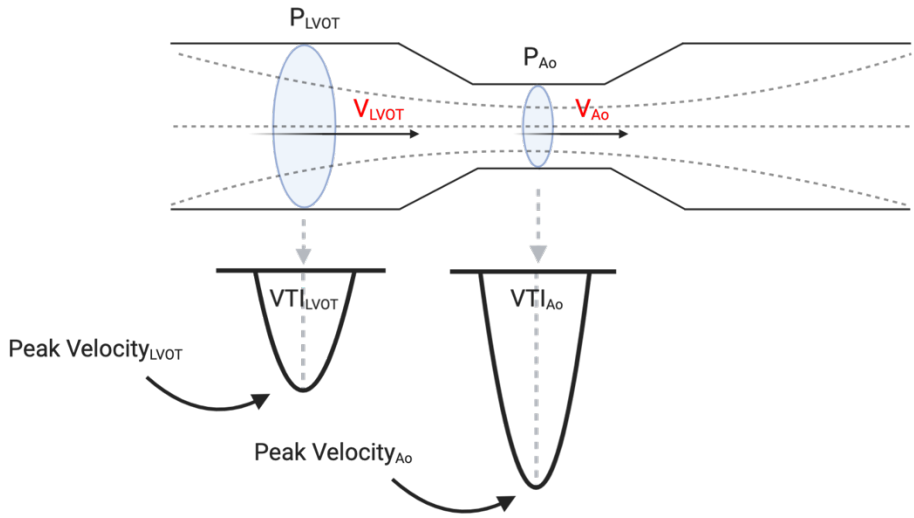

Simplification of Bernoulli Equation

$$P_{LVOT} + \tfrac{1}{2}\rho v_{LVOT}^2 + \rho g y_{LVOT} = P_{Ao} + \tfrac{1}{2}\rho v_{Ao}^2 + \rho g y_{Ao}$$

$$P_{LVOT} + \tfrac{1}{2}\rho v_{LVOT}^2 = P_{Ao} + \tfrac{1}{2}\rho v_{Ao}^2$$

$$P_{LVOT} - P_{Ao} = \tfrac{1}{2}\rho v_{Ao}^2 - \tfrac{1}{2}\rho v_{LVOT}^2$$

$$P_{LVOT} - P_{Ao} \approx \tfrac{1}{2}\rho v_{Ao}^2$$

1 mmHg = 133.3 Pa
Pa = N/m^2

$\rho_{Blood} \approx 1060\ kg/m^3$
$P = kg/m^3$

v = m/s

$$P_{LVOT\,(mmHg)} - P_{Ao\,(mmHg)} \approx \frac{\frac{1}{2}(1060\ kg/m3)}{133.3\ N/m2} \times v_{Ao(m/s)}^2$$

$$\Delta P_{(mmHg)} \approx 4v_{(m/s)}^2$$

Continuity Equation

$$AVA = \frac{Area_{LVOT} \times VTI_{LVOT}}{VTI_{Ao}}$$

Figure 15: Bernoulli Equation, Simplification, and Aortic Valve Area
Depiction of a pipe system similar to the LVOT and AV for application of the Bernoulli Equation (**A**). Simplification of the Bernoulli Equation for calculation of transaortic pressure gradient in the AV (**B**). Continuity equation for calculation of aortic valve area (**C**). Made with Biorender©.

Appendix B - Echocardiography

Figure 16: Parasternal Long Axis View
Parasternal long axis view of a mouse heart in 2D B-mode. Image analysis was completed in Vevo 3100 analysis software. LVOT diameter is assessed for AVA calculation.

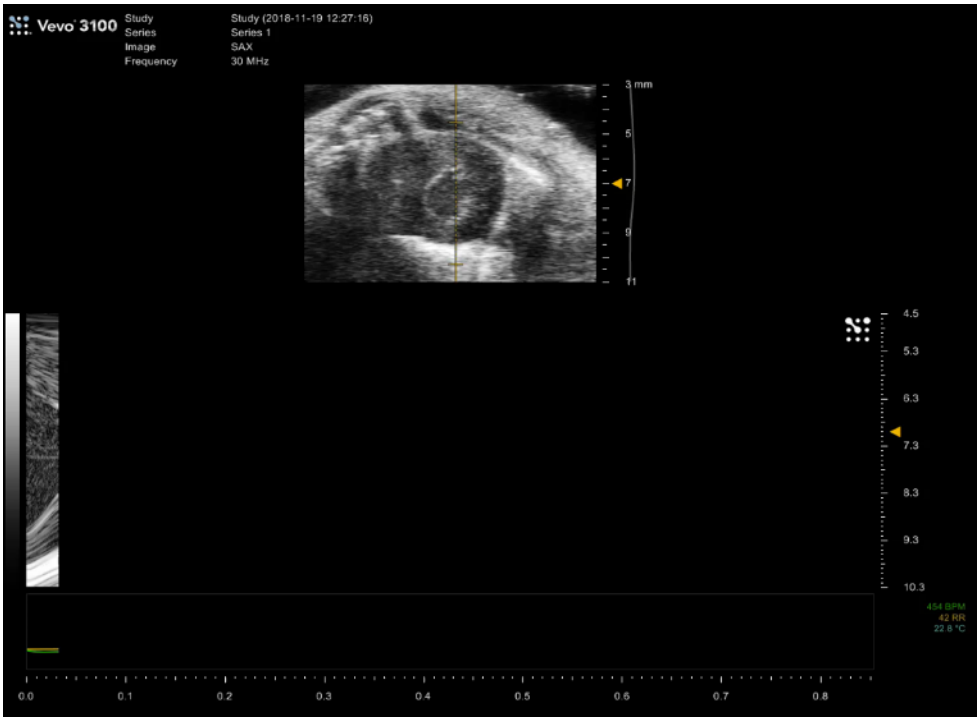

Figure 17: Parasternal Short Axis View
Parasternal short axis view of mouse heart in 2D B-mode and M-mode to assess leaflet separation (Not visible as a static image). Image analysis was completed in Vevo 3100 analysis software.

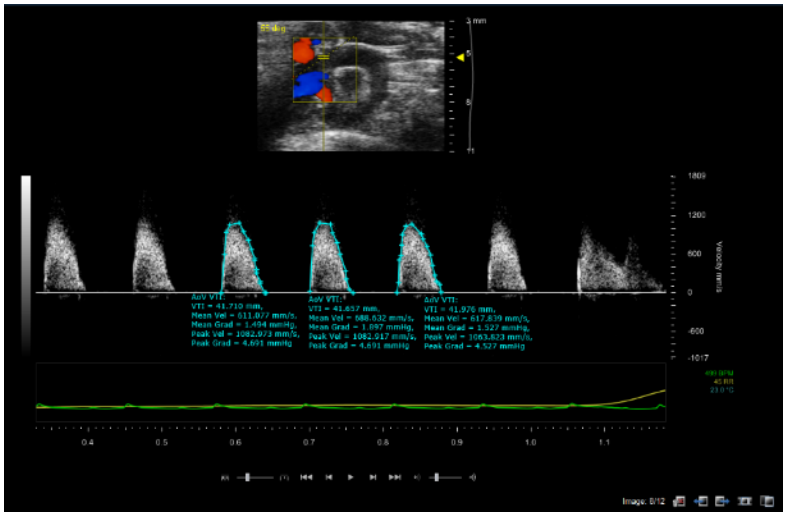

Figure 18: Pulse Wave Colour Doppler
Pulse wave colour doppler at the level of the aortic valve in a mouse with example measurements taken in order to calculate aortic valve area. Mean gradient and peak velocity are measured simultaneously. Image analysis was completed in Vevo 3100 analysis software.

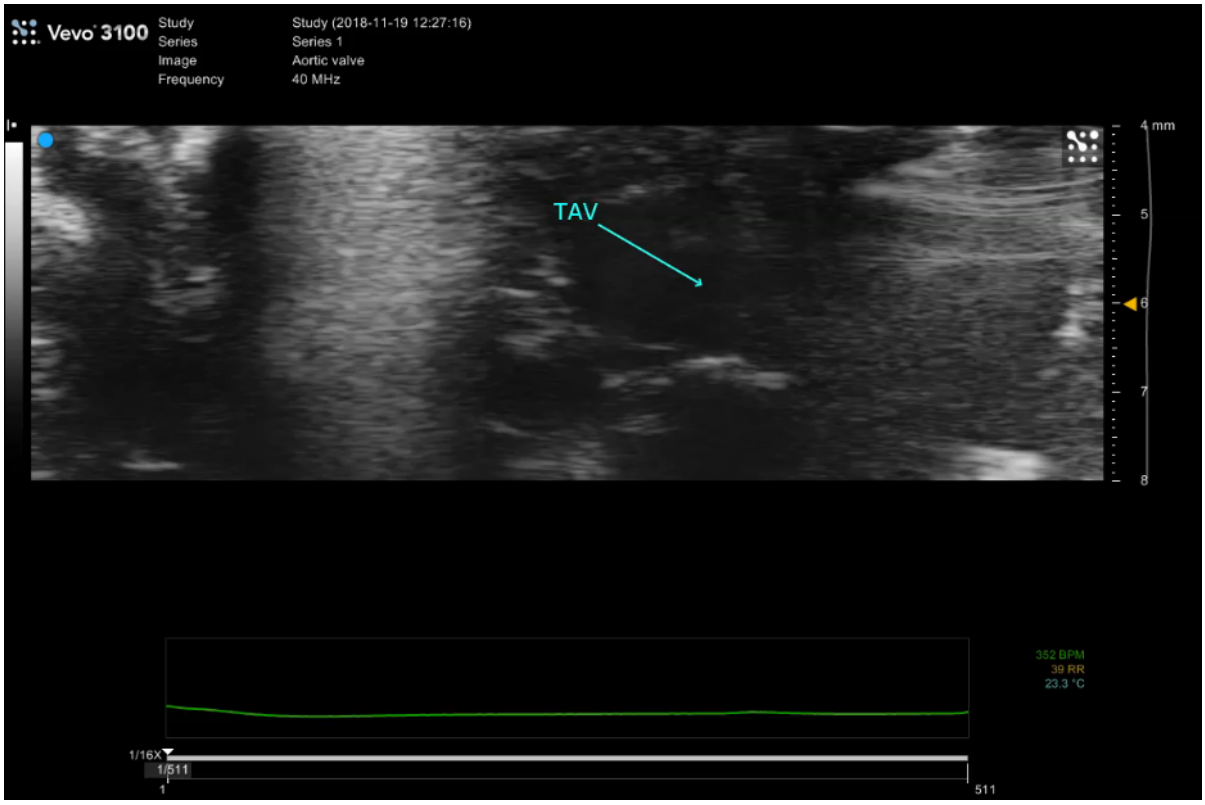

Figure 19: Valve Morphology – Tricuspid Aortic Valve
Tricuspid aortic valve in a mouse model by 2D B-mode in PSAX. Not visible as a static image. Image analysis was completed in Vevo 3100 analysis software.

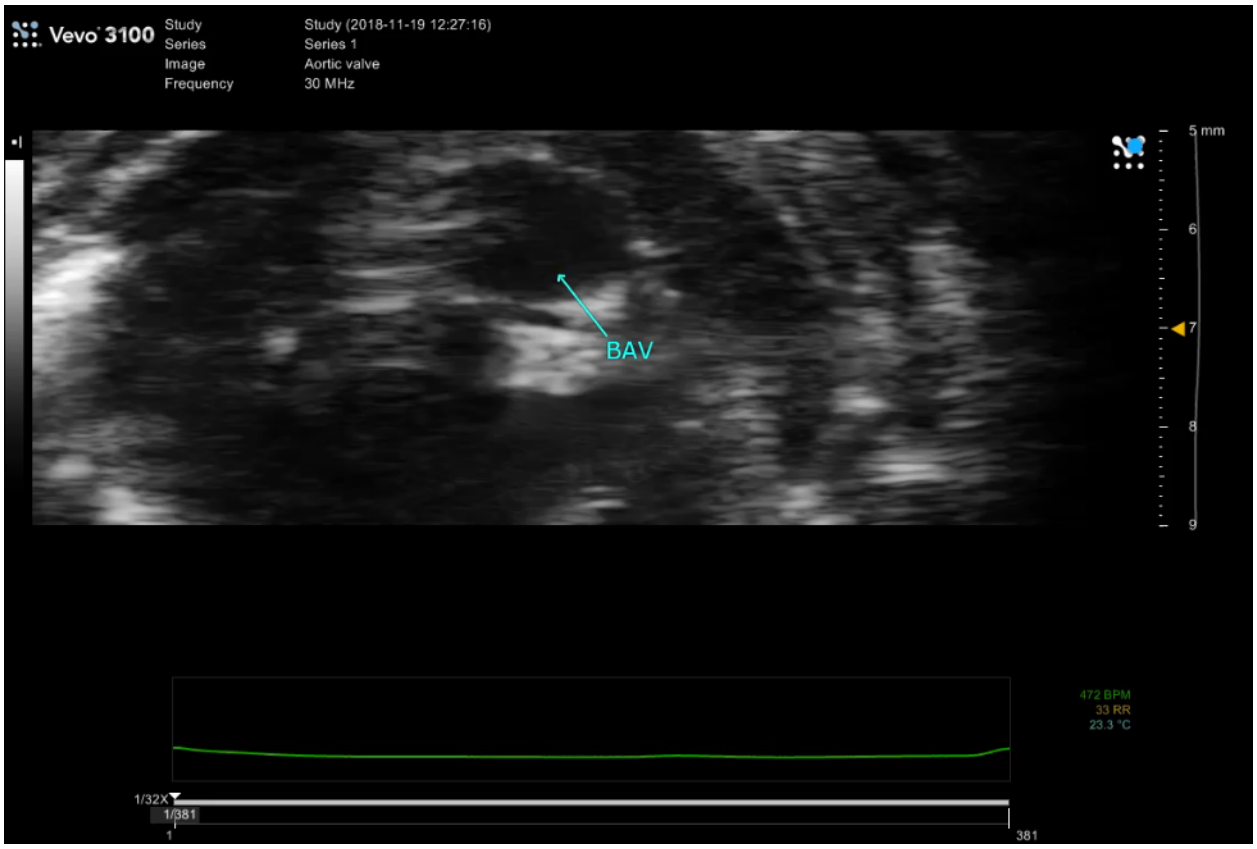

Figure 20: Valve Morphology - Bicuspid Aortic Valve
Bicuspid aortic valve in a 6-month old *Gata6* mouse by 2D B-mode in PSAX. Not visible as a static image. Image analysis was completed in Vevo 3100 analysis software.

Appendix C - Histology

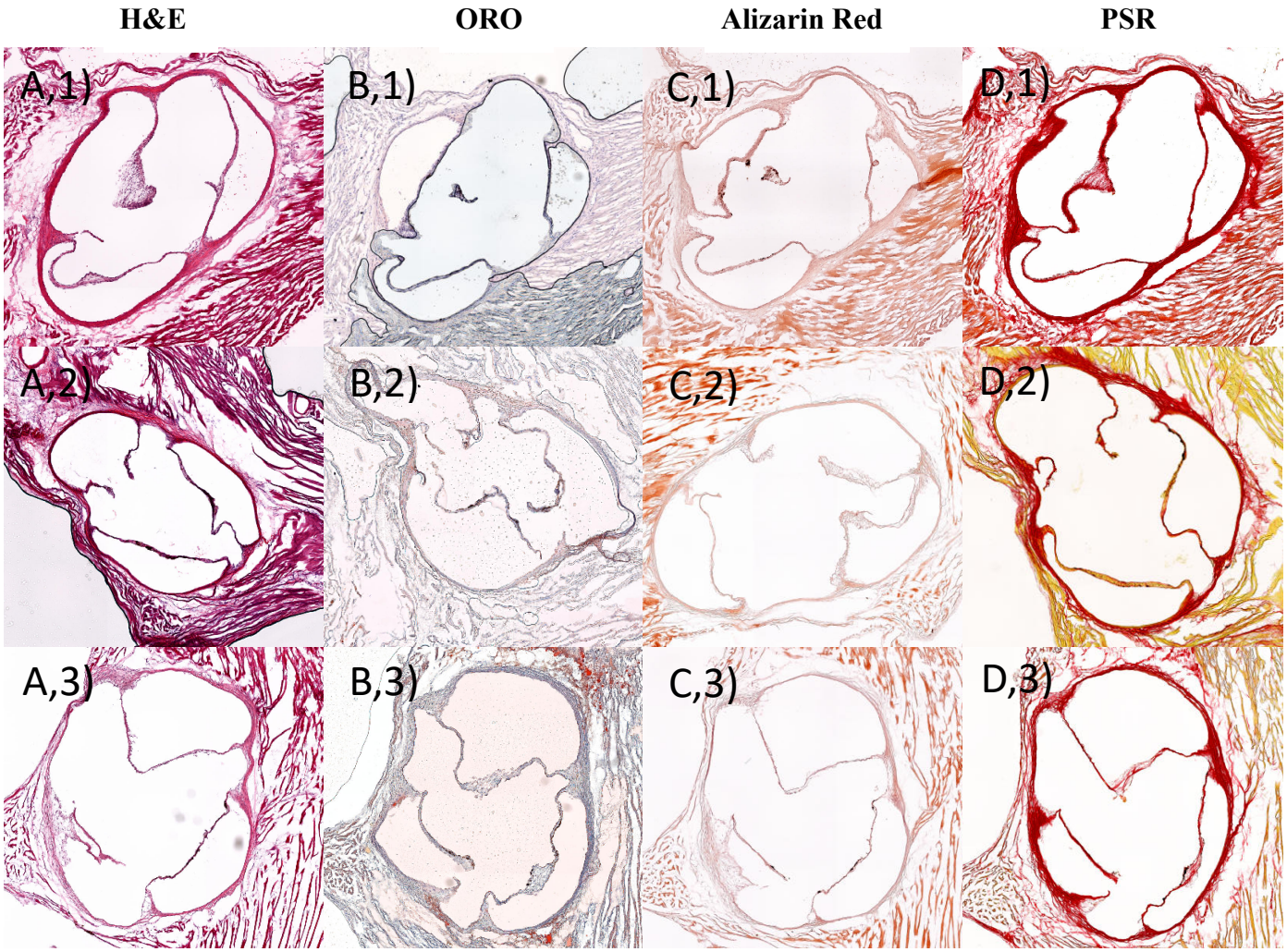

Figure 21: Histological Analysis of Various Biomarkers of Interest in WT Animals Representative histological panel indicating various biomarkers which are upregulated in the progression of CAVD. WT animals do not express quantitative measures of disease progression as is seen in the ApoE$^{-/-}$ group. Moving top to bottom represents the expression of each biomarker at either 4, 8, or 12 months, respectively. In the first panel, a representative figure of hematoxylin and eosin indicates changes in tissue morphology and leaflet thickness (**A,**). ORO indicates lipid staining within various atherosclerotic lesions which form within the aortic sinus (**B**). Alizarin red is used for the detection of microcalcifications within the lesion and leaflets, respectively (**C**). Picrosirius red is used for representation of collagen remodelling within the lesion of the aortic sinus (**D**). All images were acquired using a Leica Slide Scanner and post-processed in Apeiro ImageScope software with analysis in ImageJ. *mo = months

Appendix D - Autoradiography

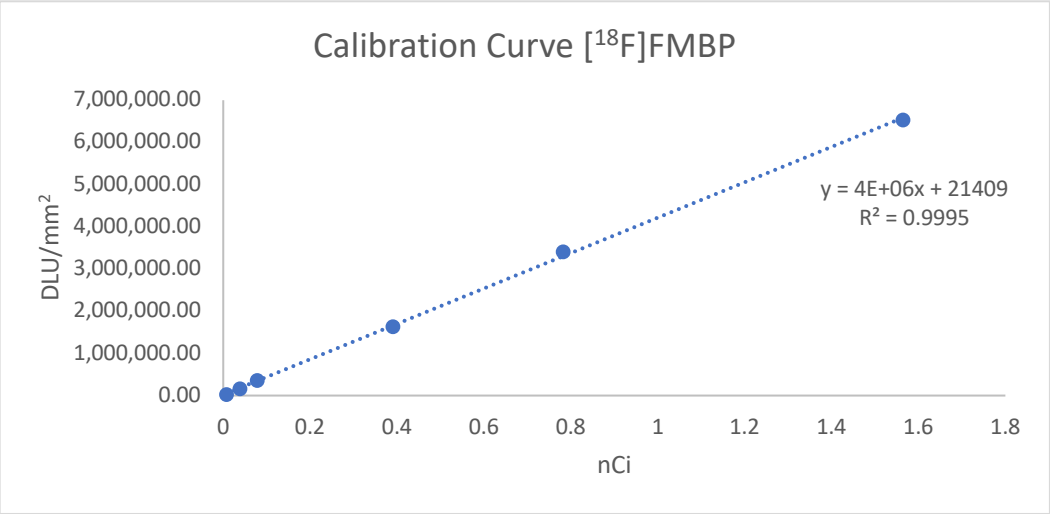

Figure 22: Calibration Curve for [^{18}F]FMBP
Autoradiography calibration curve of [^{18}F]FMBP for quantification of activity/mm^2 in tissue samples analyzed on a Phosphor screen. Calibration curves were generated by spotting a thin-layer chromatography panel with increasing amounts of a known concentration of radiotracer. This was exposed to the phosphor screen simultaneously with the samples being imaged.

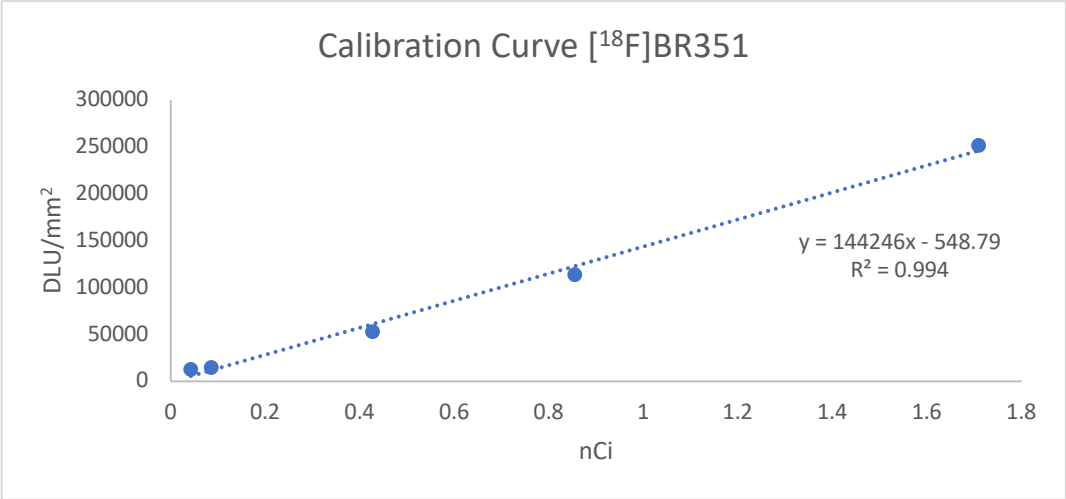

Figure 23: Calibration Curve for [^{18}F]BR351
Autoradiography calibration curve of [^{18}F]BR351for quantification of activity/mm^2 in tissue samples analyzed on a Phosphor screen. Calibration curves were generated by spotting a thin-layer chromatography panel with increasing amounts of a known concentration of radiotracer. This was exposed to the phosphor screen simultaneously with the samples being imaged.

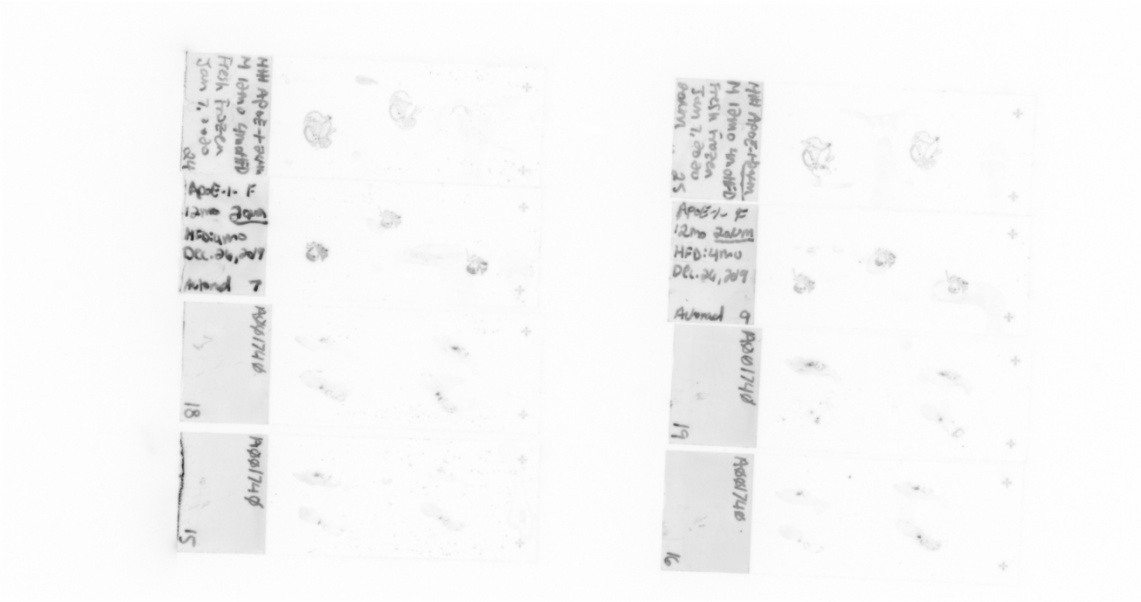

Figure 24: Autoradiography with [^{18}F]FMBP
Autoradiography was performed using [^{18}F]FMBP on 12-month ApoE$^{-/-}$ and human tissue samples of severe AS with CAVD. The tissue was incubated with 45 kBq of radiotracer for the baseline (right) and the same amount of activity was used for the block (left) with the addition of co-incubation using 2 µM of non-radioactive FMBP.

Curriculum Vitae

Contributions to Research
Publications, Presentations and Abstracts

Articles, *Peer Reviewed*

2020 *Selective Imaging of Matrix Metalloproteinase-13 to Detect Extracellular Matrix Remodeling in Atherosclerotic Lesions*. **In Preparation (May 15, 2020) – TBD**
Authors: Ariel Buchler, BSc; Maxime Munch, PhD; **Gedaliah Farber**, BHSc; Benjamin H. Rotstein PhD.
Description: Contributing author in submitted publication. Completed PET imaging studies (*in vivo* and *ex* vivo) and analysis; autoradiography (*in vivo* and *ex* vivo); biodistribution and analysis; tissue collection, preparation, staining, and analysis; experimental design and method development; manuscript composition.

2020 *The Future of Cardiac Molecular Imaging.* **In Press (March 17, 2020) – Seminars in Nuclear Medicine**
Authors: **Gedaliah Farber**, BHSc; Kevin E. Boczar, MD; Christiane C. Wiefels, MD; Jason G.E. Zelt MSc; Emel Celiker Guler, MD; Robert A. deKemp, PhD; Rob S. Beanlands, MD; and Benjamin H. Rotstein, PhD.
Description: Invited review highlighting the future of nuclear and molecular cardiac imaging.

2019 *Innate immune Nod1/RIP2 signaling is essential for cardiac hypertrophy, –but requires mitochondrial antiviral signaling protein (MAVS) for signal transductions and energy balance*. **Submitted (November 27, 2019) – Circulation**
Authors: Han-Bin Lin, PhD; Kotaro Naito, MD, PhD; Yena Oh, MSc; **Gedaliah Farber**,BHSc; Georges Kanaan, PhD; Alan Valaperti, PhD; Fayez Dawood, PhD; Liyong Zhang, PhD; Guo Hua Li, MD, PhD; David Smyth, PhD; Mark Moon, MSc; Youan Liu, MD; Kyoung-Han Kim, PhD; Benjamin Rotstein, PhD; Wenbin Liang, PhD; Dana Philpott, PhD; Mary-Ellen Harper, PhD; Peter P Liu, MD.
Description: Contributing author in submitted publication. Completed Positron Emission Tomography for glucose metabolism studies in various animal models, aided in analysis and preparation of figures.

Abstracts and Presentations at Scientific Meetings, *Peer Reviewed*

2020 *Nuclear and molecular imaging modalities for predicting calcific aortic valve disease progression in animal models* – Seminars in Nuclear Medicine and Molecular Imaging. New Orleans, USA

Description: Primary author at scientific meeting, prepare oral presentation, poster presentation, and abstract, communicate findings to scientific community.

2019 *Imaging Valvular Matrix Remodelling with PET to Predict Progression of Aortic Stenosis in Calcific Aortic Valve Disease Mouse Models* – University of Ottawa, Faculty of Medicine Discovery Day. Ottawa, Canada
Description: Communicate findings to lay public and prospective students looking to join the Faculty of Medicine graduate studies program at the University of Ottawa.

2019 *Imaging valvular matrix remodelling with PET for tracer evaluation in CAVD mouse models* – Quebec-Ontario Mini-Symposium for Synthetic and Bioorganic Chemistry. Ottawa, Canada
Description: Primary author at scientific meeting, prepared poster presentation and abstract, communicated findings to scientific community.

2019 *Development of Selective PET Radiotracers for Matrix Metalloproteinase 13* – Quebec-Ontario Mini-Symposium for Synthetic and Bioorganic Chemistry. Ottawa, Canada
Description: Second author at scientific meeting, prepared histological figures and analysis, oral presentation and poster presented to scientific community.

2019 *Imaging Valvular Matrix Remodelling with PET to Predict Progression of Aortic Stenosis in Calcific Aortic Valve Disease Mouse Models* – World Molecular Imaging Congress. Montreal, Canada
Description: Primary author at scientific meeting, prepared oral presentation and abstract, communicated findings to scientific community (Molecular imaging).

2019 *Development of Selective PET Radiotracers for Matrix Metalloproteinase 13* – Canadian Chemistry Conference and Exhibition. Quebec City, Canada
Description: Third author at scientific meeting, prepared histological figures and analysis, poster presented to scientific community.

2019 *Imaging Valvular Matrix Remodelling with PET to Predict Progression of Aortic Stenosis in Calcific Aortic Valve Disease Mouse Models* – Ottawa Cardiovascular Research day. Ottawa, Canada
Description: Primary author at scientific meeting, prepared presentation and abstract, communicated findings to scientific community (abstract).

2019 *Imaging Valvular Matrix Remodelling with PET to Predict Progression of Aortic Stenosis in Calcific Aortic Valve Disease Mouse Models* – Toronto-Ottawa Heart Summit. Ottawa, Canada
Description: Primary author at scientific meeting, prepared presentation and abstract, communicated findings to scientific community (cardiology).

2019 *Imaging Valvular Matrix Remodelling with PET to Predict Progression of Aortic Stenosis in Calcific Aortic Valve Disease Mouse Models* – BMI Poster Day. Ottawa, Canada
Description: Primary author at scientific meeting, prepared presentation and abstract, communicated findings to scientific community.

Honours, Scholarships and Awards

2019 **CIHR: Institute Community Support – Travel Award**
Description: CIHR travel grant to present first author research at the scientific meeting *Seminars in Nuclear Medicine and Molecular Imaging* in New Orleans, Louisiana. Competition unkown.

2019 **World Molecular Imaging Congress: Oral Poster Award**
Description: First prize in Cardiology at the World Molecular Imaging Congress for the oral poster presentation amongst 40 other presenters. International scientific meeting with over 400 posters presented by researchers in various molecular imaging fields. Prize of $250 USD.

2019 **University of Ottawa Graduate and Postdoctoral Studies Travel Grant**
Description: $300 CAD to cover costs of presenting first author research at a scientific meeting.

2019 **Queen Elizabeth II Graduate Scholarship in Science and Technology**
Description: Encourages and supports the best students involved in science and technology research and funds one year of study. Students must show high academic achievement (minimum GPA of 8.0/10) and have made significant research contributions. Unknown number of applicants, 41 awards allocated to University of Ottawa graduate students, assessed competitively. Value: $15,000 CAD.

2018 **Canadian Graduate Scholarship – Masters (CIHR)**
Description: Funding for one year of graduate studies at the masters level. Students must show high academic standing, research potential, and interpersonal skills. 417 awards given across Canada, 16 allocated to the University of Ottawa. Unknow number of applicants, assessed competitively. Value: $17,500 CAD.

2018 - 2020 **University of Ottawa Excellence Scholarship** (Value: $7,500 CAD/year x2)

Volunteer Activities

2019 **University of Ottawa Graduate Studies – Scholarship Workshop Mentor**
Description: As a previous CIHR and QEII grant holder, review graduate student scholarship material for major internal and external funding opportunities. Aid in application preparation in order to help student applications stand out to funding agencies.

2019 **Discover and Engage in the Graduate REsearch Experience (DEGREE) Shadowing Program Mentor**
Description: Engage and expose undergraduate students to research and motivate them to pursue undergraduate research opportunities.

2019 - Present **Student Mentorship**: 5 Students
Description: Mentor and engage undergraduate students in research, problem-solving, safe lab practices, and ethics. Design independent projects, aid in presenting results.

2019 **UOHI Trainee Committee** – Social Coordinator
Description: Organize and lead social, research and professional development events for hospital trainees. Aid in and vote on committee matters, represent the hospital on a community and international scale, communicate with hospital leaders and healthcare decision makers.

2018 **UOHI Research Photographer**
Description: Take professional-quality photos of trainees for hospital promotion and personal professional endeavours, edit and vet photos, deliver publication-quality edits to administrative staff in a timely manner.

Additional Project Contributions and Collaborations

2020 **Imaging calcification with PET via [^{18}F]NaF in mgp$^{-/-}$ mice**
Principle Investigator: Dr. Alex Stewart

2019 **Development of Selective PET Radiotracers for Matrix Metalloproteinase-13**
Principle Investigator: Dr. Benjamin Rotstein

2019 **Perfusion and cardiac metabolism in post-MI animal models to evaluate biomaterial therapy**
Principle Investigator: Dr. Erik Suuronen

2019 **Investigating dual therapy with Metformin and DPP4 inhibitors to attenuate adverse cardiac effect after myocardial infarction**
Principle Investigator: Dr. Erin Mulvihill

2019 **Detection and quantification of atherosclerotic plaques in ApoE$^{-/-}$ via echocardiography**
Principle Investigator: Dr. Erin Mulvihill